

AN ULTRAVIOLET SPECTROSCOPIC ATLAS OF LOCAL STARBURSTS AND STAR-FORMING GALAXIES: THE LEGACY OF FOS AND GHRS

CLAUS LEITHERER¹, CHRISTY A. TREMONTI², TIMOTHY M. HECKMAN³, AND DANIELA CALZETTI⁴

¹ Space Telescope Science Institute, 3700 San Martin Drive, Baltimore, MD 21218, USA; leitherer@stsci.edu

² Department of Astronomy, University of Wisconsin-Madison, 475 N. Charter St., Madison, WI 53706, USA; tremonti@astro.wisc.edu

³ Department of Physics & Astronomy, Johns Hopkins University, Homewood Campus, Baltimore, MD 21218, USA; heckman@pha.jhu.edu

⁴ Department of Astronomy, University of Massachusetts, LGRT-B 524, Amherst, MA 01003, USA; calzetti@astro.umass.edu

Received 2010 August 17; accepted 2010 October 31; published 2011 January 5

ABSTRACT

We present 46 rest-frame ultraviolet (UV) spectra of 28 local starburst and star-forming galaxies which were observed with the Faint Object Spectrograph (FOS) and the Goddard High Resolution Spectrograph (GHRS) of the *Hubble Space Telescope* (*HST*) at a spectral resolution of a few 100 km s⁻¹. We compare the *HST* spectra with lower resolution *International Ultraviolet Explorer* (*IUE*) spectra of the same galaxies and find systematic differences: the bright star clusters targeted in *HST*'s $\sim 1''$ apertures provide about 15% of the starburst luminosity traced by *IUE*'s $10'' \times 20''$ aperture; they are bluer and have stronger stellar-wind features suggesting that the *HST* apertures have preferentially been placed on the youngest areas of the burst. In contrast, lines arising from the interstellar medium (ISM) show similar equivalent widths in both the large and small aperture observations, suggesting similar ISM properties from larger to smaller scales. In order to quantify the UV spectral morphology of star-forming galaxies, we created a set of UV line indices similar to the standard optical Lick indices. We discuss the relation between the UV spectral morphology and the properties of the galaxy host. We present our atlas of FOS and GHRS spectra both in print and online. The data set is useful as a baseline for comparisons with observations of the rest-frame UV spectra of star-forming galaxies at high redshift.

Key words: atlases – galaxies: high-redshift – galaxies: starburst – galaxies: stellar content – line: profiles – ultraviolet: galaxies

Online-only material: color figures

1. MOTIVATION

While our understanding of galaxy formation and evolution is in many ways incomplete, it has become increasingly evident that much of the stellar mass in the universe was assembled in violent and short-lived episodes of star formation at high redshift (e.g., Papovich et al. 2001; Shapley et al. 2001; Pérez-González et al. 2008). In the latter half of the Hubble time, the overall star formation rate of the universe has declined precipitously (Lilly et al. 1996; Cowie et al. 1999; Hopkins 2004). Nevertheless, there remain present-day examples of galaxies undergoing intense bursts of star formation. Indeed, while few in number, these starburst galaxies are responsible for $\sim 20\%$ of the entire high-mass star formation in the local universe (Brinchmann et al. 2004). Local starburst galaxies provide us with an opportunity to investigate in detail a phenomenon with profound cosmic consequences.

In this study, we examine the UV spectral properties of 28 local starburst galaxies which were observed with the Faint Object Spectrograph (FOS) and the Goddard High Resolution Spectrograph (GHRS) instruments on board the *Hubble Space Telescope* (*HST*). The rest-frame UV is of particular interest because it is the window onto the high-redshift universe provided by large ground-based telescopes working in the visible. Our study complements the earlier work of Kinney et al. (1993) and Heckman et al. (1998; hereafter H98) based on spectra obtained with the *International Ultraviolet Explorer* (*IUE*) satellite. It also provides guidance for population synthesis work that attempts to model the UV spectra of star-forming galaxies theoretically (Leitherer et al. 2010). While the majority of our sample galaxies were included in the earlier *IUE* analysis, substantial

differences between the *HST* and *IUE* observations motivate our present undertaking. The velocity resolution of our FOS and GHRS data (a few 100 km s⁻¹) represents nearly a factor of 10 improvement over that of *IUE* in low-dispersion mode, enabling us to make use of the spectral *line profile* information and allowing us to study the kinematics of the interstellar medium (ISM). In addition, the *HST* apertures employed in our sample observations have projected sizes more than a factor of 10 smaller than that of *IUE*, often encompassing only a few bright star clusters. Thus, our study provides a small-scale probe of the ISM and stellar populations, which we compare to the more global view offered by *IUE*.

In this paper, we present a UV spectral atlas of *HST* observations and consider the differences inherent in the *HST* and *IUE* spectra due to the different spatial scales sampled. We take advantage of the superior resolution and signal-to-noise of the *HST* spectra and of the availability of multi-wavelength data for our local sample to perform a thorough analysis of the connection between a starburst's UV spectral morphology and its luminosity and dust content and the mass and metallicity of its host galaxy.

In Section 2, we review the origin of the prominent spectral features in the UV and the conclusions of previous studies of UV starburst spectra based on *IUE* data. The 46 *HST* galaxy spectra which constitute our sample are presented in Section 3, as are the details of the data compilation and reduction procedures. A key element in unlocking the diagnostic power of the rest-frame UV is the availability of multi-wavelength data for our local starburst sample. In Section 4, we describe the UV, optical, infrared (IR), and H I observations which we use to infer the starburst luminosity and dust content, as well as the host galaxy

mass and metallicity. We compare the *IUE* and *HST* spectra in Section 5. A new set of standard UV indices is introduced in Section 6. In Section 7, we discuss the correlation of the UV features with the physical properties of the galaxies. Finally, Section 8 presents our conclusions.

2. BACKGROUND

Data obtained early in the *IUE* mission demonstrated the existence of a rich absorption spectrum in star-forming galaxies (Weedman et al. 1981; Huchra et al. 1983). The identification of prominent UV spectral features with lines seen in massive stars provided some of the first *direct* evidence for the presence of large numbers of massive stars in actively star-forming galaxies. The vastly better sensitivity and spectral resolution of *HST*'s instruments brought subsequent advances in detecting and classifying the stellar and interstellar spectral features (e.g., Heckman & Leitherer 1997; Vázquez et al. 2004).

The space-UV lines observed in starburst galaxies are essentially of four types: stellar-wind features, stellar photospheric absorption lines, interstellar absorption lines, and nebular emission lines. In Table 1, we provide a comprehensive compilation of the four types of lines over the wavelength range 1150–3000 Å. Many of the listed lines may not be observable in typical UV spectra of a starburst galaxy. However, our goal is to provide the community with a database that is as complete as possible for comparison with a wide variety of data. The table lists the atom or ion (Column 1) and is arranged by the laboratory vacuum wavelength (Column 2). Columns 3 and 4 give the ionization (E_{ion}) and excitation (E_{exc}) energies for the preceding ionization stage and the lower excitation level, respectively. These are the relevant quantities for the formation of almost all observed features, except for recombination lines like He II $\lambda 1640$, for which the upper $E_{\text{ion}} = 54.4$ eV matters. Crosses in Columns 5–8 indicate whether the lines predominantly form in the wind, the stellar photosphere, the ISM, and/or have a nebular origin, respectively. The distinction between these categories is sometimes not unique, as low-ionization resonance lines could be both interstellar and stellar. Therefore, we used *typical* FOS and GHRS starburst spectra to guide our categorization scheme. The references are listed in Column 9.

The most prominent features are typically the N V $\lambda 1240$, Si IV $\lambda 1400$, and C IV $\lambda 1550$ stellar-wind lines, which are produced in the expanding atmospheres of O and B stars. They are broad (~ 2000 km s $^{-1}$), blueshifted (by ~ 1000 km s $^{-1}$), and often show a P-Cygni profile. Because these lines are produced in a radiatively driven wind which must overcome the gravitational well of the mass-losing star, the line strength and profile shape have a mass dependence and can be used as a tracer of the initial mass function (IMF) and star formation history. However, the line profile is also metallicity sensitive since both stellar evolution and mass loss have a strong metallicity dependence (Kudritzki & Puls 2000; Puls et al. 2008).

Stellar photospheric features abound shortward of ~ 2000 Å, where O- and B-star spectra exhibit heavy line blanketing, primarily by transitions of highly ionized iron and nickel (Dean & Bruhweiler 1985; Brandt et al. 1998). Among the multitude of photospheric lines, there are a handful of well-developed features (e.g., C III $\lambda 1176$, O IV $\lambda 1342$, Fe V $\lambda 1363$, Si III $\lambda 1417$, C III $\lambda\lambda 1426/28$, S V $\lambda 1502$), many of which are comprised of groups of neighboring lines. However, these features are typically quite weak in contrast with the stellar-wind lines. Because their equivalent widths (EW) range from < 1 to a few Å (as compared to 5–15 Å for the wind lines), high signal-to-noise

(S/N) moderate resolution spectra are required. Nonetheless, the photospheric features are of interest because they provide another tracer of the young stellar population. Rix et al. (2004) used theoretical models to calibrate several weak photospheric features as metallicity indicators. This method was used by Halliday et al. (2008) to determine the stellar metallicity of star-forming galaxies at redshift $z \approx 2$.

The ISM also leaves a pronounced imprint on the space-UV spectra of galaxies. Strong interstellar absorption lines are produced by the resonance transitions of the abundant ionic species: H I, C II, C IV, N I, N V, O I, Al II, Al III, Si II, Si III, Si IV, Mg I, Mg II, and Fe II. These lines appear optically thick (on the flat part of the curve of growth), and therefore their strength is primarily determined by the velocity dispersion of the starburst and the covering factor of the ISM. The ISM absorption lines offer a unique probe of the kinematics of the gas over a broad range in ionization.

Nebular emission lines are also present in the UV, although their EWs are typically small in all but the lowest metallicity galaxies. The most prominent lines are C III] $\lambda\lambda 1907/09$ and Si III] $\lambda\lambda 1883/92$. The C III] line can be used in concert with some of the weaker lines—ideally O III] $\lambda\lambda 1661/66$ —to derive the C/O abundance ratio (Kobulnicky & Skillman 1998; Garnett et al. 1999).

While the UV spectra of star-forming galaxies are rich in stellar absorption lines which are sensitive to age and metallicity, the low-order shape of the continuum is surprisingly robust to these parameters (quite unlike the case in the optical). The shape of the spectrum can be parameterized by a power law ($F_\lambda \propto \lambda^\beta$) between 1200 and 3000 Å. When stars younger than about 10 Myr are present, the value of β exhibits a narrow range of values between -2.7 and -2.5 (Meurer et al. 1997; Calzetti 2001). The relative insensitivity of the UV continuum to the particulars of the stellar population turns out to be fortunate happenstance because this part of the spectrum is extremely sensitive to dust. Even a modest extinction of $A_V = 1$ implies a factor of 10 dimming around 2000 Å. However, starburst galaxies appear to obey a well-defined wavelength-dependent reddening law which accounts for the net effects of dust/star geometry, scattering, and total absorption (Calzetti 2001). Thus, if the presence of massive stars can be ascertained from the stellar absorption lines, the dust content can be estimated by comparing the observed power law index of the continuum to the expected intrinsic one.

The sheer diversity of the spectral features in the space UV makes the diagnostic power of this spectral region unparalleled. However, at present few empirical tools exist to help mine the information. In this paper, we focus on developing automated techniques for extracting the maximum information from UV spectra. Our sample of nearby starbursts is ideal for calibrating UV diagnostics of galaxy physical properties since their properties are generally already well known from detailed observations in a number of wavebands.

An important milestone in the study of star-forming galaxies was the creation of a catalog of UV spectra by Kinney et al. (1993). The sample comprised 143 nearby $\lesssim 100$ Mpc spiral, irregular, blue compact, Seyfert 2, LINER, and starburst galaxies with spectra available in the *IUE* archives. *IUE* was ideal for characterizing the UV properties of these nearby galaxies because its $10'' \times 20''$ aperture was large enough to encompass the central few kiloparsecs of most objects. Besides laying the ground work for many more detailed studies, Kinney et al. presented the first qualitative picture of the UV

Table 1
UV Spectral Lines Observed in Star-forming Galaxies

Ion	λ_{lab} (Å)	E_{ion} (eV)	E_{exc} (eV)	Wind	Photo	ISM	Nebular	Reference
C I	1157.19	0.00	0.00			+		1
N IV	1168.60	47.45	52.08		+			2
C IV	1168.87	47.89	40.28		+			2
C IV	1168.99	47.89	40.28		+			2
N IV	1169.06	47.45	52.08		+			2
N IV	1169.48	47.45	52.08		+			2
C III	1175.53	24.38	6.50	+	+			3
N III	1183.03	29.60	18.09		+			4
N III	1184.54	29.60	18.10		+			4
Mn II	1199.39	7.44	0.00			+		1
N I	1199.55	0.00	0.00			+		1
N I	1200.22	0.00	0.00			+		1
N I	1200.71	0.00	0.00			+		1
Si III	1206.50	16.35	0.00			+		1
H I	1215.67	0.00	0.00			+		1
N V	1238.82	77.47	0.00	+		+		1
N V	1242.80	77.47	0.00	+		+		1
C III	1247.38	24.38	12.69		+			5
S II	1250.58	10.36	0.00			+		1
S II	1253.81	10.36	0.00			+		1
Si II	1260.42	8.15	0.00			+		1
C I	1277.24	0.00	0.00			+		1
Si III	1294.54	16.35	6.55		+			5
C III	1296.33	24.38	33.48		+			6
Si III	1296.74	16.35	6.54		+			5
Si III	1298.93	16.35	6.57		+			5
O I	1302.17	0.00	0.00			+		1
Si II	1304.37	8.15	0.00			+		1
Ni II	1317.22	7.64	0.00			+		1
C II	1323.93	11.26	9.29		+			6
N III	1324.35	29.60	33.13		+			6
C I	1328.83	0.00	0.00			+		1
C II	1334.53	11.26	0.00			+		1
C II*	1335.71	11.26	0.01			+		1
O IV	1341.64	54.93	22.40		+			4
Fe V	1345.61	54.80	28.99		+			4
Fe V	1362.86	54.80	26.84		+			4
Fe V	1363.08	54.80	23.20		+			4
Fe V	1364.82	54.80	23.15		+			4
O V	1371.30	77.41	19.69		+			3
Si IV	1393.76	33.49	0.00	+		+		1
Si IV	1402.77	33.49	0.00	+		+		1
Si III	1417.24	16.35	10.28		+			5
C III	1426.45	24.38	29.53		+			5
Fe V	1427.27	54.80	26.49		+			4
C III	1427.85	24.38	29.53		+			5
Fe V	1430.44	54.80	23.36		+			4
Ni II	1454.84	7.64	0.00			+		1
Co II	1466.21	7.86	0.00			+		1
Ni II	1467.26	7.64	0.00			+		1
Ni II	1467.76	7.64	0.00			+		1
C III	1478.00	24.38	33.47		+			3
N IV]	1486.50	47.45	0.00	+			+	3
S V	1501.76	47.30	15.77		+			5
Si II	1526.71	8.15	0.00			+		1
Fe IV	1530.04	30.65	15.89		+			4
Si II*	1533.43	8.15	0.04			+		1
C IV	1548.19	47.89	0.00	+		+		1
C IV	1550.77	47.89	0.00	+		+		1
C I	1560.31	0.00	0.00			+		1
C I*	1560.68	0.00	0.00			+		1
Fe II	1608.45	7.87	0.00			+		1
Fe II	1611.20	7.97	0.00			+		1
C III	1620.40	24.38	32.20		+			3
He II	1640.42	24.59	40.81	+			+	3
C I	1656.93	0.00	0.00			+		1
C I*	1657.38	0.00	0.00			+		1

Table 1
(Continued)

Ion	λ_{lab} (Å)	E_{ion} (eV)	E_{exc} (eV)	Wind	Photo	ISM	Nebular	Reference
C I*	1657.91	0.00	0.00			+		1
O III]	1660.81	35.12	0.01				+	3
Fe V	1662.32	54.80	24.20		+			4
O III]	1666.15	35.12	0.04				+	3
Al II	1670.79	5.99	0.00			+		1
Ni II	1709.60	7.64	0.00			+		1
Fe IV	1717.90	30.65	17.15		+			4
N IV	1718.55	47.45	16.20	+	+			6
Ni II	1741.55	7.64	0.00			+		1
Ni II	1751.91	7.64	0.00			+		1
Si II	1808.01	8.15	0.00			+		1
Si I	1845.52	0.00	0.00			+		1
Al III	1854.72	18.83	0.00	+		+		1
Al III	1862.79	18.83	0.00	+		+		1
Si III]	1883.00	16.35	0.00				+	3
Si III]	1892.03	16.35	0.00				+	3
Fe II	1901.77	7.87	0.00			+		1
C III]	1906.68	24.38	0.00				+	3
C III]	1908.73	24.38	0.00				+	3
Fe III	1922.79	16.16	7.87		+			3
Fe III	1923.01	16.16	10.28		+			3
Fe III	1923.88	16.16	8.21		+			3
Fe III	1924.53	16.16	9.50		+			3
Fe III	1926.04	16.16	8.21		+			3
Fe III	1926.30	16.16	3.71		+			3
Fe III	1930.39	16.16	7.87		+			3
Fe III	1931.51	16.16	8.64		+			3
Fe III	1932.82	16.16	10.29		+			3
Fe III	1949.67	16.16	10.33		+			3
Fe III	1950.33	16.16	11.03		+			3
Fe III	1951.01	16.16	8.76		+			3
Fe III	1952.65	16.16	8.77		+			3
Fe III	1953.33	16.16	8.77		+			3
Fe III	1954.61	16.16	8.77		+			3
Fe III	1958.59	16.16	8.21		+			3
Fe III	1960.32	16.16	9.86		+			3
Fe III	1962.72	16.16	8.65		+			3
Fe III	1964.15	16.16	8.65		+			3
Fe III	1966.41	16.16	8.66		+			3
Zn II	2026.14	9.39	0.00			+		1
Cr II	2026.27	6.77	0.00			+		1
Mg I	2026.48	0.00	0.00			+		1
Cr II	2056.25	6.77	0.00			+		1
N II]	2140.00	14.53	0.02				+	3
C III	2163.61	24.38	34.28	+				3
Fe II	2249.88	7.87	0.00			+		1
Fe II	2260.78	7.87	0.00			+		1
C III	2297.58	24.38	12.69	+				6
[O III]	2321.66	35.12	0.01				+	3
C II]	2326.00	11.26	0.00				+	3
[O III]	2331.00	35.12	0.04				+	3
Fe II	2344.21	7.87	0.00			+		1
Fe II	2374.46	7.87	0.00			+		1
Fe II	2382.76	7.87	0.00			+		1
[O II]	2470.97	13.62	0.00				+	3
[O II]	2471.09	13.62	0.00				+	3
Mn II	2576.88	7.44	0.00			+		1
Fe II	2586.65	7.87	0.00			+		1
Mn II	2594.50	7.44	0.00			+		1
Fe II	2600.17	7.87	0.00			+		1
Mn II	2606.46	7.44	0.00			+		1
Mg II	2796.35	7.65	0.00			+		1
Mg II	2803.53	7.65	0.00			+		1
Mg I	2852.96	0.00	0.00			+		1

References. (1) Prochaska et al. 2001; (2) Robert et al. 2003; (3) This work; (4) Brandt et al. 1998; (5) de Mello et al. 2000; (6) Pettini et al. 2000.

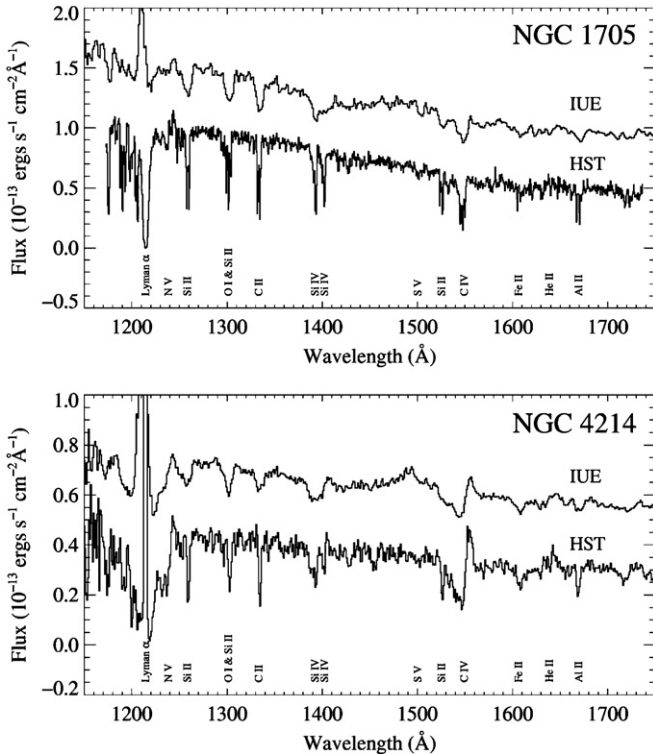


Figure 1. Comparison of *IUE* and *HST* spectra of NGC 1705 (upper) and NGC 4214 (lower). The *IUE* spectrum has been scaled so that the flux at 1500 \AA matches the *HST* spectrum and then offset by 0.5 (top) and 0.3 (bottom) for clarity. The slightly blueshifted lines visible in the *HST* spectrum of NGC 1705 are due to interstellar absorption from the Milky Way.

spectra of galaxies of different morphological types and activity classes.

H98 undertook a more quantitative study of a subset of 45 starburst galaxies in the sample of Kinney et al. (1993). This work explored the connection between the UV spectral morphology of the starbursts and the mass, metallicity, luminosity, and dust content of their host galaxies. While the majority of the strong UV spectral features were well known by the time of H98, the modest spectral resolution and S/N of the *IUE* spectra precluded detailed analysis of individual lines. Figure 1 shows two examples of the very best quality *IUE* spectra and their corresponding FOS and GHRS spectra. *IUE*'s 6 \AA ($\sim 1200 \text{ km s}^{-1}$) resolution is barely sufficient to distinguish between the broad stellar-wind lines and the much narrower stellar photospheric and interstellar features. Some features which show up clearly in the *HST* spectrum, for example Si II $\lambda 1526$, become blended with neighboring lines—including foreground Milky Way lines—in the *IUE* spectrum (see NGC 1705 in Figure 1, in particular). Because of this, and the generally modest S/N of the *IUE* spectra, H98 chose to characterize the UV spectral morphology of their starbursts with three parameters: β , the slope of the UV continuum between 1250 and 1850 \AA ; W_{IS} , the average EW of the strongest low-ionization interstellar features Si II $\lambda 1260$, O I $\lambda 1302 +$ Si II $\lambda 1304$, C II $\lambda 1335$; and W_{W} , the average of the Si IV $\lambda 1400$ and C IV $\lambda 1550$ lines, which contain potentially large contributions from stellar winds.

The simple parameterization of the UV spectral features adopted by H98 proved adequate to elucidate fundamental trends in UV spectral morphology with galaxy physical parameters. The spectral parameters β , W_{IS} , and W_{W} were found

to be correlated with the strength and dustiness of the starburst, and the luminosity, mass, and metallicity of the host galaxy. Starbursts were shown to occupy a very small part of the available parameter space: more luminous starbursts tended to occur in more massive, metal-rich hosts, and consequently their spectra exhibited more dust reddening and stronger UV lines. This finding was a major leap forward in our understanding of the physical parameter space occupied by starbursts and their host galaxies, and it provided a framework for interpreting rest-frame UV observations of high-redshift galaxies.

Our present undertaking is motivated by goals similar to that of H98, namely the development of tools for analyzing spectra of high-redshift galaxies. However, the ensuing years have brought major improvements in the data available at both low and high redshift, thanks to the availability of UV spectrographs on board *HST* and the improved light gathering power of ground-based telescopes. This has enabled us to explore the UV spectral morphology of galaxies with more detail and sophistication. We therefore revisit some of the correlations outlined by H98 with an improved parameterization of the UV spectral features.

The FOS and GHRS were two of the four original axial instruments aboard *HST*. Both instruments were removed from *HST* and replaced by the Space Telescope Imaging Spectrograph (STIS) during Servicing Mission 2 in 1997 February. STIS operates in the UV as well and is currently still operational. It is complemented by the Cosmic Origins Spectrograph (COS), which was installed during Servicing Mission 4 in 2009 May. The two legacy instruments FOS and GHRS have left behind a rich and self-contained data set whose calibration is complete and final. The spatial sizes of their apertures ($1'' - 2''$) are an order of magnitude *smaller* than that of *IUE*, yet they are an order of magnitude *larger* than those of the STIS apertures typically employed ($0''.2$). Ongoing STIS observations, by virtue of their spatial sampling, often focus on individual star clusters in starburst galaxies, whereas FOS and GHRS spectra encompass small starburst regions having sizes of $\sim 100 \text{ pc}$ (corresponding to $2''$ at 10 Mpc). This makes the FOS and GHRS data set the sample of choice for our study.

3. OBSERVATIONS

3.1. The Sample

Our sample is composed of 28 local starburst and star-forming galaxies with high-quality UV spectra available from the *HST* archive. Because of the small size of the *HST* apertures (1 to a few arcseconds), our spectral atlas includes multiple pointings within many of the sample galaxies, for a total of 46 unique spectra⁵. Of these, 29 were obtained with the FOS and 17 with the GHRS. The characteristics of the FOS and GHRS instruments are described in Sections 3.2 and 3.3, respectively. Details of the individual observations which constitute our sample are given in Table 2. The entries in this table are as follows: Column 1: spectrum identifier used in this paper; Column 2: host galaxy name; Column 3: name of the starburst region; Columns 4 and 5: right ascension and declination of the region (note that the absolute pointing of *HST* has typical systematic uncertainties of $\sim 1''$); Column 6: instrument used⁶; Column 7: grating used; Column 8: aperture used; Column 9:

⁵ We count multiple wavelength settings at the same pointing as one spectrum.

⁶ See <http://www.stsci.edu/documents/dhb/pdf/FOS.pdf> and http://www.stsci.edu/instrument-news/handbooks/ghrs/GHRS_1.html for descriptions of the FOS and GHRS, respectively.

Table 2
Summary of *HST* Observations

ID	Galaxy	Region	R. A. (h:m:s)	Decl. (d:m:s)	Instrument	Grating	Aperture	Program	Wavelength (Å)	S/N
A	NGC 1068	Knot2	02:42:40.3	-00:00:38	GHRS	G140L	LSA	3024	1164–1451	1
A	NGC 1068	Knot2	02:42:40.3	-00:00:38	GHRS	G140L	LSA	3024	1493–1780	3
A	NGC 1068	POS1	02:42:40.3	-00:00:38	GHRS	G140L	LSA	5942	1165–1461	9
A	NGC 1068	POS3	02:42:39.9	-00:00:45	GHRS	G140L	LSA	5942	1165–1461	2
A	NGC 1068	POS4	02:42:41.4	-00:00:37	GHRS	G140L	LSA	5942	1166–1462	2
A	NGC 1068	POS8A	02:42:39.9	-00:00:58	GHRS	G140L	LSA	5942	1165–1461	2
B	SBS 0335–052		03:37:44.0	-05:02:39	GHRS	G140L	LSA	6678	1162–1448	9
C	NGC 1569	A	04:30:48.2	+64:50:59	FOS	G130H	B-2	6408	1087–1606	2
C	NGC 1569	A	04:30:48.2	+64:50:59	FOS	G190H	B-2	6408	1572–2312	5
C	NGC 1569	A	04:30:48.2	+64:50:59	FOS	G270H	B-2	6408	2222–3277	9
D	NGC 1705		04:54:13.4	-53:21:39	GHRS	G140L	SSA	5691	1175–1462	13
D	NGC 1705		04:54:13.4	-53:21:39	GHRS	G140L	SSA	5691	1453–1740	9
E	NGC 1741	Offset	05:01:37.7	-04:15:29	GHRS	G140L	LSA	5738	1175–1461	10
E	NGC 1741	Offset	05:01:37.7	-04:15:29	GHRS	G140L	LSA	5738	1453–1739	6
F	NGC 2366	NGC 2363	07:28:42.6	+69:11:22	FOS	G190H	C-1	5246	1571–2311	7
F	NGC 2366	NGC 2363 CP1-A	07:28:42.6	+69:11:22	FOS	G130H	B-3	6096	1087–1606	5
F	NGC 2366	NGC 2363 CP1-B	07:28:43.5	+69:11:23	FOS	G130H	B-3	6096	1087–1606	11
G	NGC 2403	VS9	07:36:28.6	+65:33:49	FOS	G190H	B-3	6044	1571–2311	10
G	NGC 2403	VS9	07:36:28.6	+65:33:49	FOS	G270H	B-3	6044	2221–3277	14
G	NGC 2403	VS38	07:36:52.1	+65:36:49	FOS	G190H	B-3	6044	1571–2311	9
G	NGC 2403	VS38	07:36:52.1	+65:36:49	FOS	G270H	B-3	6044	2221–3277	11
G	NGC 2403	VS44	07:37:06.8	+65:36:39	FOS	G190H	B-3	6044	1571–2311	13
G	NGC 2403	VS44	07:37:06.8	+65:36:39	FOS	G270H	B-3	6044	2221–3277	19
H	He 2–10	A	08:36:15.1	-26:24:34	GHRS	G140L	LSA	6580	1314–1600	14
H	He 2–10	B	08:36:15.8	-26:24:35	GHRS	G140L	LSA	6580	1314–1601	6
I	IRAS 08339+6517		08:38:23.0	+65:07:14	GHRS	G140L	LSA	5954	1213–1500	11
I	IRAS 08339+6517		08:38:23.0	+65:07:14	GHRS	G140L	LSA	5954	1466–1753	9
J	SBS 1415+437		14:17:01.4	+43:30:05	FOS	G190H	B-3	5408	1572–2312	5
K	IZw18		09:34:02.1	+55:14:27	FOS	G190H	B-3	3840	1572–2312	5
K	IZw18	NW HIIR	09:34:02.0	+55:14:28	FOS	G190H	C-1	5434	1571–2311	7
K	IZw18	SE HIIR	09:34:02.3	+55:14:23	FOS	G190H	B-3	6536	1572–2312	5
L	NGC 3690		11:28:30.8	+58:33:43	FOS	G130H	B-3	4250	1087–1606	4
L	NGC 3690		11:28:30.8	+58:33:43	FOS	G190H	B-3	4250	1573–2330	9
M	UM 469	POS1	11:57:12.5	+02:28:29	FOS	G190H	B-3	6801	1572–2312	9
M	UM 469	POS1	11:57:12.5	+02:28:29	FOS	G270H	B-3	6801	2222–3277	12
N	NGC 4038	405 updated	12:01:50.4	-18:52:12	GHRS	G140L	LSA	5962	1314–1601	7
N	NGC 4038	442 updated	12:01:53.0	-18:52:08	GHRS	G140L	LSA	5962	1314–1601	3
O	NGC 4214		12:15:39.3	+36:19:36	FOS	G130H	B-3	4122	1087–1606	8
O	NGC 4214		12:15:39.3	+36:19:36	FOS	G130H	B-3	4122	1573–2330	13
P	Tololo 1214–277		12:17:17.1	-28:02:32	GHRS	G140L	LSA	6678	1175–1461	3
P	Tololo 1214–277		12:17:17.1	-28:02:32	FOS	G190H	B-3	3840	1572–2312	1
Q	NGC 4569		12:36:49.8	+13:09:46	FOS	G130H	B-3	6112	1087–1606	6
Q	NGC 4569		12:36:49.8	+13:09:46	FOS	G190H	B-3	6112	1572–2312	16
Q	NGC 4569		12:36:49.8	+13:09:46	FOS	G270H	B-3	6112	2222–3277	29
R	IC 3639		12:40:52.9	-36:45:22	GHRS	G140L	LSA	6539	1162–1449	5
R	IC 3639		12:40:52.9	-36:45:22	GHRS	G140L	LSA	6539	1301–1588	6
S	NGC 4670		12:45:17.2	+27:07:32	FOS	G130H	B-3	4250	1087–1606	9
S	NGC 4670		12:45:17.2	+27:07:32	FOS	G190H	B-3	4250	1573–2330	12
T	NGC 4861	POS1	12:59:00.3	+34:50:44	FOS	G190H	B-3	6801	1572–2312	6
T	NGC 4861	POS1	12:59:00.3	+34:50:44	FOS	G270H	B-3	6801	2222–3277	7
U	NGC 5055		13:15:49.3	+42:01:46	FOS	G130H	B-2	6112	1087–1606	1
U	NGC 5055		13:15:49.3	+42:01:46	FOS	G190H	B-2	6112	1572–2312	5
U	NGC 5055		13:15:49.3	+42:01:46	FOS	G270H	B-2	6112	2222–3277	14
V	NGC 5135		13:25:44.0	-29:50:01	GHRS	G140L	LSA	6539	1162–1449	6
V	NGC 5135		13:25:44.0	-29:50:01	GHRS	G140L	LSA	6539	1313–1600	6
W	NGC 5253	HII-1	13:39:56.0	-31:38:26	FOS	G190H	B-3	6021	1572–2312	5
W	NGC 5253	HII-2	13:39:56.0	-31:38:24	FOS	G190H	B-3	6021	1572–2312	4
W	NGC 5253	UV1	13:39:55.8	-31:38:27	FOS	G130H	B-3	6001	1087–1606	3
W	NGC 5253	UV1	13:39:55.8	-31:38:27	FOS	G190H	B-3	6001	1572–2312	5
W	NGC 5253	UV1	13:39:55.8	-31:38:27	FOS	G270H	B-3	6001	2222–3277	5
W	NGC 5253	UV2	13:39:55.9	-31:38:32	FOS	G130H	B-3	6001	1087–1606	3
W	NGC 5253	UV2	13:39:55.9	-31:38:32	FOS	G190H	B-3	6001	1572–2312	5
W	NGC 5253	UV2	13:39:55.9	-31:38:32	FOS	G270H	B-3	6001	2222–3277	5
W	NGC 5253	UV3	13:39:55.4	-31:38:30	FOS	G130H	B-3	6001	1087–1606	2
W	NGC 5253	UV3	13:39:55.4	-31:38:30	FOS	G190H	B-3	6001	1572–2312	4
W	NGC 5253	UV3	13:39:55.4	-31:38:30	FOS	G270H	B-3	6001	2222–3277	5

Table 2
(Continued)

ID	Galaxy	Region	R. A. (h:m:s)	Decl. (d:m:s)	Instrument	Grating	Aperture	Program	Wavelength (Å)	S/N
X	Tololo 1345–420	POS1	13:48:22.3	−42:21:15	FOS	G190H	B-3	6801	1572–2312	3
X	Tololo 1345–420	POS1	13:48:22.3	−42:21:15	FOS	G270H	B-3	6801	2222–3277	5
Y	NGC 5457	NGC 5455	14:03:01.2	+54:24:27	FOS	G190H	C-1	6044	1571–2311	9
Y	NGC 5457	NGC 5455	14:03:01.2	+54:24:27	FOS	G270H	C-1	6044	2221–3277	13
Y	NGC 5457	Searle5	14:02:55.0	+54:22:26	FOS	G130H	B-3	3813	1087–1606	3
Y	NGC 5457	Searle5	14:02:55.0	+54:22:26	FOS	G190H	B-3	3813	1573–2330	3
Y	NGC 5457	Searle5	14:02:55.0	+54:22:26	FOS	G270H	B-3	3813	2221–3301	4
Y	NGC 5457	NGC 5471	14:04:29.0	+54:23:49	FOS	G190H	C-1	6044	1573–2330	3
Y	NGC 5457	NGC 5471	14:04:29.0	+54:23:49	FOS	G270H	C-1	6044	2221–3301	4
Z	NGC 7130		21:48:19.5	−34:57:05	GHRS	G140L	LSA	6539	1175–1462	6
Z	NGC 7130		21:48:19.5	−34:57:05	GHRS	G140L	LSA	6539	1314–1601	6
AA	NGC 7552		23:16:10.8	−42:35:03	FOS	G130H	B-3	4250	1087–1606	7
AA	NGC 7552		23:16:10.8	−42:35:03	FOS	G190H	B-3	4250	1573–2330	12
BB	NGC 7714		23:36:14.1	+02:09:18	GHRS	G140L	LSA	6672	1175–1461	10
BB	NGC 7714		23:36:14.1	+02:09:18	GHRS	G140L	LSA	6672	1402–1689	10

HST program ID; Column 10: wavelength region covered; and Column 11: measured S/N per pixel. *HST* images of our sample galaxies with the spectroscopic apertures overlaid are shown in the Appendix.

Our sample was culled from all of the FOS and GHRS spectra available in the *HST* archive. We included all spectra of star-forming or Seyfert 2 galaxies observed both pre- and post-COSTAR which met the following criteria:

1. Wavelength coverage of at least 250 Å between 1150 and 3200 Å in the galaxy rest frame.
2. Spectral resolution of 0.5–3 Å.
3. S/N of at least 2 in the continuum in the combined spectrum.
4. Clear evidence of spectral features caused by star formation. (This criterion eliminates all but a handful of Seyfert 2 galaxies.)

Despite the unsystematic selection inherent in this archival sample, the galaxies span a fairly broad swath of parameter space. They include a wide range of morphological types (irregulars, nuclear starbursts, blue compact dwarfs) and activity classes (H II galaxies, LINERS, Seyfert 2's), and encompass a broad range of global galaxy parameters such as metallicity and absolute blue magnitude (see Section 4 for details). Since both the FOS and GHRS instruments have completed their mission lifetimes, this sample represents their legacy.

3.2. FOS

The FOS (Harms et al. 1979) operated on board *HST* for six years beginning with the telescope's launch in 1990. The FOS had two independent optical channels which focused spectral images on the photocathodes of photon-counting Digicon detectors. The detector on the red side was sensitive from 1620 to 8500 Å, while the detector on the blue side was sensitive from 1150 to 5400 Å. Dispersers were available for both high ($\lambda/\Delta\lambda = 1300$) and low ($\lambda/\Delta\lambda = 250$) resolution modes. The data that met our selection criterion were obtained at high resolution using the G130H, GH190H, or G270H gratings, on either the red or blue sides. The G130H grating provided a dispersion of ~ 1.00 Å per diode in the 1140–1606 Å regime; the G190H, ~ 1.45 Å per diode from 1590 to 2312 Å; and the G270H, ~ 2.05 Å per diode from 2222 to 3277 Å.

The spectral resolution depends on the dispersion of the grating, the aperture used, and the degree to which the source fills the aperture. Table 2 lists the configuration employed for each observation. The apertures range from 0''.26 to 1''.0, with the 06''.86 circular aperture being the most common. (Note that the introduction of the COSTAR optics caused a 16% scale change, such that the original 1'' aperture was reduced to 0''.86.) The degree to which our spectroscopic targets—generally bright star clusters—resemble point or extended sources is difficult to estimate due to the redshift range of our sample and the highly inhomogeneous nature of starburst galaxies. A spectral line from an object uniformly filling the 0''.86 circular aperture would have a FWHM of 2.29 Å, whereas a point source would yield a FWHM of ~ 1 Å. The resolutions of the FOS spectra in our sample will fall in between these extremes.

The FOS target acquisition could achieve a pointing accuracy of 0''.1–0''.2 for a point source (There will still be the systematic *HST* pointing uncertainty of $\sim 1''$). However, the inhomogeneous nature of our starburst galaxies induces greater uncertainty in the process. We note here that the object coordinates listed in Table 2 and shown in Figure A1 are the input coordinates; the final pointing of *HST* could differ by a few arcseconds.

We re-calibrated our FOS spectra by running the Post Operational Archive version of the FOS calibration pipeline (POA_CALFOS v1.2.1). POA_CALFOS performs all of the tasks of the original CALFOS pipeline with some enhancements. Most significantly, the accuracy of the wavelength zero point on the FOS/BLUE side is restored to its original specification of ± 1 pixel. The standard pipeline reduction begins with a correction for dead diodes, geomagnetic induced image motion, and saturation in the detector electronics. The data are then dark subtracted, scattered light corrected, flat fielded, and corrected for aperture throughput and time-dependent instrumental sensitivity variations. Finally, a dispersion solution is constructed, and the spectra are converted into absolute flux units of $\text{erg s}^{-1} \text{cm}^{-2} \text{\AA}^{-1}$.

After pipeline reprocessing, we boxcar smoothed the spectra by 5 pixels to recover the original sampling of the diodes. We combined multiple observations acquired at the same pointing with the same grating by averaging the spectra weighted by their exposure times with the IRAF task spcombine.

3.3. GHRS

The GHRS (Brandt et al. 1994) was also one of the first-generation science instruments on board *HST*. It was designed to complement FOS by providing higher resolution and throughput in the UV, at the expense of more limited wavelength coverage. Like FOS, GHRS had two channels with different photocathode sensitivities: side 1, which was optimized in the far-UV ($\sim 1050\text{--}1700 \text{\AA}$) and side 2, which was optimized in the near-UV ($\sim 1700\text{--}3200 \text{\AA}$). The GHRS spectra in our sample were obtained with the G140L grating which provided a dispersion of $\sim 0.57 \text{\AA}$ per pixel over a 285\AA variable bandpass in the $1100\text{--}1900 \text{\AA}$ range. Two science apertures were available: the $2.\prime 0$ square Large Science Aperture (LSA; $1.\prime 74$ post-COSTAR) and the $0.\prime 25$ Small Science Aperture (SSA; $01.\prime 22$ post-COSTAR). All of our sample observations, with the exception of those of NGC 1705, were made through the Large Science Aperture. The resolution of a point source observed with the G140L grating through the LSA is $\sim 0.9 \text{\AA}$, which corresponds to $\sim 250 \text{ km s}^{-1}$ at 1100\AA and $\sim 140 \text{ km s}^{-1}$ at 1900\AA . The resolution of a fully extended source observed through the LSA is degraded by a factor of four since four GHRS diodes are encompassed by the LSA. Our spectra have resolutions in between these extremes, generally closer to the point-source value.

The target acquisition generally succeeded in peaking up on the bright knots of star formation targeted in our sample galaxies. However, due to the nature of the process, the acquisition input coordinates recorded in Table 2 and shown in Figure A1 should not be considered accurate to more than a few arcseconds.

We recalibrated our GHRS data by re-running the standard CALHRS reduction pipeline with an updated set of reference files. The standard reduction begins by computing the count rate per pixel and then correcting for non-uniform diode sensitivity and for the finite response time of the detector electronics. The spectrum's location on the photocathode is then mapped out and a correction is applied for vignetting. In order to fully sample the *HST* point-spread function, the diodes were sub-sampled by moving the spectrum on the detector by a fraction of a diode and storing the spectra separately. These sub-sampled spectra are recombined by the pipeline. The spectrum's position on the photocathode is then converted into a wavelength, and the wavelength zero point is adjusted for the appropriate aperture and corrected to the heliocentric system. The detector background is subtracted off and a sensitivity vector is applied to convert the spectrum from counts per second per diode to absolute flux units of $\text{erg s}^{-1} \text{cm}^{-2} \text{\AA}^{-1}$.

After pipeline re-processing, we recomputed the wavelength zero point of the spectrum if supporting “SPYBAL” observations were available with the STSDAS IRAF task `waveoff`. For NGC 1068, sub-integrations acquired in FP-SPLIT mode were aligned and combined using the STSDAS IRAF tasks `poffsets` and `specalign`. In cases where multiple observations were acquired at the same pointing, we averaged the spectra weighted by their exposure times using the IRAF task `scombine`.

3.4. Correcting the Wavelength Zero Points

The wavelength calibration of the FOS and GHRS spectra is expected to be accurate to ± 1 diode, or about ~ 1.5 and $\sim 0.5 \text{\AA}$, respectively. To improve the wavelength calibration, we cross-correlated each spectrum with a zero-velocity template. We constructed the templates individually for each spectrum. When far-UV spectra were available, we compared them with

Table 3
Milky Way Lines

Line	Wavelength (\AA)	$W_v (\text{km s}^{-1})$	$\sigma (\text{km s}^{-1})$
Si III 1206	1206.50	180.0	25.0
S II 1253	1253.81	70.0	90.0
S II 1260	1260.42	190.0	65.0
O I 1302	1302.17	105.0	55.0
S II 1304	1304.37	95.0	35.0
C II 1334	1334.53	160.0	45.0
Si IV 1393	1393.76	60.0	40.0
Si IV 1402	1402.77	40.0	10.0
Si II 1526	1526.71	95.0	25.0
C IV 1548	1548.20	80.0	25.0
C IV 1550	1550.77	45.0	20.0
Al II 1670	1670.79	115.0	30.0
Si II 1808	1808.01	50.0	30.0
Al III 1854	1854.72	55.0	20.0
Zn II 2026	2026.14	55.0	30.0
Zn II 2062	2062.66	35.0	20.0
Fe II 2344	2344.21	95.0	25.0
Fe II 2374	2374.46	75.0	20.0
Fe II 2382	2382.77	110.0	30.0
Fe II 2586	2586.65	80.0	25.0
Fe II 2600	2600.17	100.0	30.0
Mg II 2796	2796.35	125.0	35.0
Mg II 2803	2803.53	115.0	25.0
Mg II 2852	2852.96	50.0	15.0

Starburst99 synthetic spectra (Leitherer & Chen 2009; Leitherer et al. 2010) for a range of ages and selected the model which produced the best fit (for details see, e.g., Tremonti et al. 2001). We redshifted this template to the heliocentric velocity of the galaxy using redshifts obtained from the NASA/IPAC Extragalactic Database (NED). We then added the foreground Milky Way absorption lines listed in Table 3 to the template assuming a velocity width of 200 km s^{-1} . The entries in this table are the median and standard deviation of the velocity EWs along various Milky Way sightlines as reported by Savage et al. (2000); see Section 3.5 for further information about the Milky Way lines. Unfortunately, the strongest features in the galaxy spectra—the stellar-wind lines and the interstellar lines—are sometimes blueshifted relative to the stellar photospheric lines, and hence are not useful for wavelength calibration. We masked these features and derived the wavelength zero points from the remaining pixels by doing a cross-correlation in real space (rather than Fourier space). The zero point is thus set by a combination of photospheric lines and Milky Way lines. The latter are used only when they are not blended with the intrinsic ISM lines ($v_{\text{helio}} > 800 \text{ km s}^{-1}$). We assumed zero velocity for the Milky Way lines, i.e., a negligible contribution by Galactic high-velocity clouds. Each cross-correlation was examined by eye. We estimate the remaining error in the far-UV zero points to be of order $\pm 0.3 \text{\AA}$.

The FOS spectra obtained in the near-UV necessitated a different procedure. The wavelength range covered by the G190H grating ($1600\text{--}2300 \text{\AA}$) does not contain any strong Milky Way lines; however, it does contain some prominent photospheric features and the C III] $\lambda\lambda 1907/09$ emission line. Unfortunately, the empirical stellar libraries used by Starburst99 do not extend beyond 1850\AA . To extend the wavelength coverage of the models out to 2200\AA , we used some fully theoretical OB-star spectra (Leitherer et al. 2010). We synthesized template spectra at ages of 1 and 5 Myr, and made a by-eye assessment of which model provided the best fit to each spectrum. To this template

we added a C III] emission line in cases where it was apparent in the data. Because C III] is not a resonance line, we assumed it to be free of the complex radiative transfer effects and at rest with respect to the stars. These templates provided reasonably good fits to most of the data with the exception of NGC 3690, NGC 4670, and NGC 7552, whose data exhibited strong photospheric features not evident in the models. For these spectra we used a near-UV STIS spectrum of He 2–10 (Chandar et al. 2003) which shows similar photospheric features as a template. In a few cases where the S/N was not adequate no correction was made. We estimate the remaining errors in the near-UV wavelength zero points to be of order $\pm 0.5 \text{ \AA}$.

In the wavelength range covered by the FOS G270H grating (2300–3200 \AA), few strong photospheric features exist, but there are a large number of strong interstellar lines. For these spectra we constructed templates using the Milky Way lines and the intrinsic interstellar absorption lines. Because many of the interstellar lines are strong and saturated, the Milky Way and intrinsic features are often blended. Where possible, we masked the intrinsic lines and used only the Milky Way lines.

After correcting the wavelength zero points, we rebinned the spectra to a common wavelength grid with a linear dispersion of 1.0 \AA for the FOS spectra and 0.57 \AA for the GHRS spectra. We merged FOS observations taken with different gratings weighting each segment by the standard deviation in the overlap region (1590–1606 \AA and 2220–2310 \AA). The agreement of the data in the overlap regions is generally quite good. However, the decline in grating throughput in these regions causes the spectra to be fairly noisy, particularly at the $\sim 1600 \text{ \AA}$ junction.

3.5. Correcting for Galactic Contamination

To obtain accurate measurements the UV spectral properties of galaxies, it is desirable to remove any contribution to the spectrum from airglow or the Milky Way foreground absorption. The ISM of the Milky Way causes both discrete and continuous absorption in the UV—line absorption due to resonance transitions of ions in the gas and continuum absorption due to dust.

A detailed analysis of Milky Way absorption lines has been carried out as part of *HST* Quasar Absorption Line Key Project (Savage et al. 2000). Using 83 FOS spectra of quasars, Savage et al. measured the velocity EWs ($W_v = cW_\lambda/\lambda$) of 29 ionic species in the range 1150–3200 \AA . This study showed the Milky Way halo to be a mixed ionization system, with the low and intermediate ions having high EWs ($W_v = 180 \text{ km s}^{-1}$) and the high ionization ions (Si IV and C IV) having weaker absorption ($W_v = 60 \text{ km s}^{-1}$). Most of the low ionization Milky Way lines are saturated, and therefore their EWs reflect the kinematical complexity of the sight line. Variations from sight line to sight line were $\sim 30\%$.

The pattern of ISM absorption lines caused by the Milky Way is very similar to that seen in more actively star-forming galaxies. This has unfortunate consequences for the spectroscopy of low-redshift galaxies because the foreground Galactic lines blend with the intrinsic ISM lines. This contamination affects nine galaxies (18 spectra) in our sample which have velocities in the range $\pm 600 \text{ km s}^{-1}$. In the remaining galaxies, the foreground lines are also problematic, because they mar regions of good continuum adjacent to the ISM lines. We have therefore attempted to remove the Milky Way lines from all of our spectra. Due to the limited positional information available on the Milky Way ISM lines, we chose to correct our spectra using the median of the EWs reported by Savage et al. (2000). We

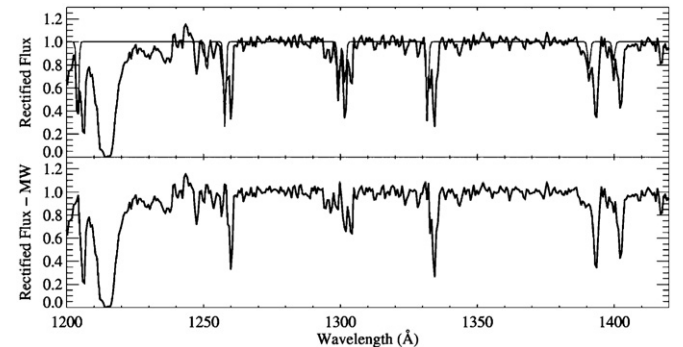


Figure 2. Spectrum of NGC 1705. The upper panel illustrates the correction that we make for the foreground Milky Way absorption (light gray line), and the lower panel shows the spectrum after subtraction of the Milky Way lines.

performed this correction by subtracting off Gaussians centered at $v = 0$ whose widths are set to the approximate instrumental resolution. The Milky Way absorption lines that we correct for are listed in Table 3.

Figure 2 shows the spectrum of NGC 1705 before and after correction for Milky Way absorption. In this high-resolution ($\sim 0.6 \text{ \AA}$) spectrum, the Milky Way absorption lines are clearly visible just slightly blueward of the starburst ISM lines. The agreement between our estimates of the foreground absorption and that seen in the spectrum (top panel) is remarkably good. This level of concordance is very typical of our spectra, although there are relatively few cases where this can be assessed reliably because the

Milky Way lines tend to be heavily blended with features in the rich starburst spectrum. The importance of the foreground absorption correction is illustrated by comparing the upper and lower panels of Figure 2. At the lower resolution typical of most of our spectra ($\sim 2 \text{ \AA}$), the Milky Way lines would clearly blend with the starburst lines and account for nearly half of the line width. In the weakest-lined galaxies in our sample, the foreground absorption correction reduces the interstellar line flux by nearly 100%. The correction to the high ionization stellar-wind lines is typically much smaller.

Each galaxy's spectral energy distribution is also modified by Galactic foreground reddening. We used the $E(B-V)$ value derived from the dust maps of Schlegel et al. (1998) and the Galactic extinction curve of Fitzpatrick (1999) to deredden the starburst spectra. The reddening corrections are relatively modest for all of our galaxies ($E(B-V) \lesssim 0.1$) with the exception of NGC 1569 ($E(B-V) \approx 0.5$). Nevertheless, a few spectra show hints of a residual in the 2175 \AA dust feature, which is most likely a consequence of a slight error in the foreground reddening correction. For NGC 1569 and I Zw 18 we adopted improved $E(B-V)$ values derived from detailed analysis of the stellar populations with *HST* (Angeretti et al. 2005; Aloisi et al. 2007).

Besides the Milky Way absorption, our starburst spectra were also contaminated by airglow emission from Earth's atmosphere, namely Ly α at 1216 \AA and O I at 1304 \AA (and occasionally [O II] $\lambda 2470$, and two unidentified lines at $\lambda 2137$ and $\lambda 2802$). Unfortunately, the strength of the airglow features is not a simple function of position on the sky, but depends sensitively on the solar angle, the column of Earth atmosphere along the line of sight, and the solar activity cycle. We therefore made no attempt to remove these features. The Ly α airglow has a sufficiently strong equivalent EW (100–1000 \AA) that it precludes analysis of the underlying starburst Ly α emission and absorption

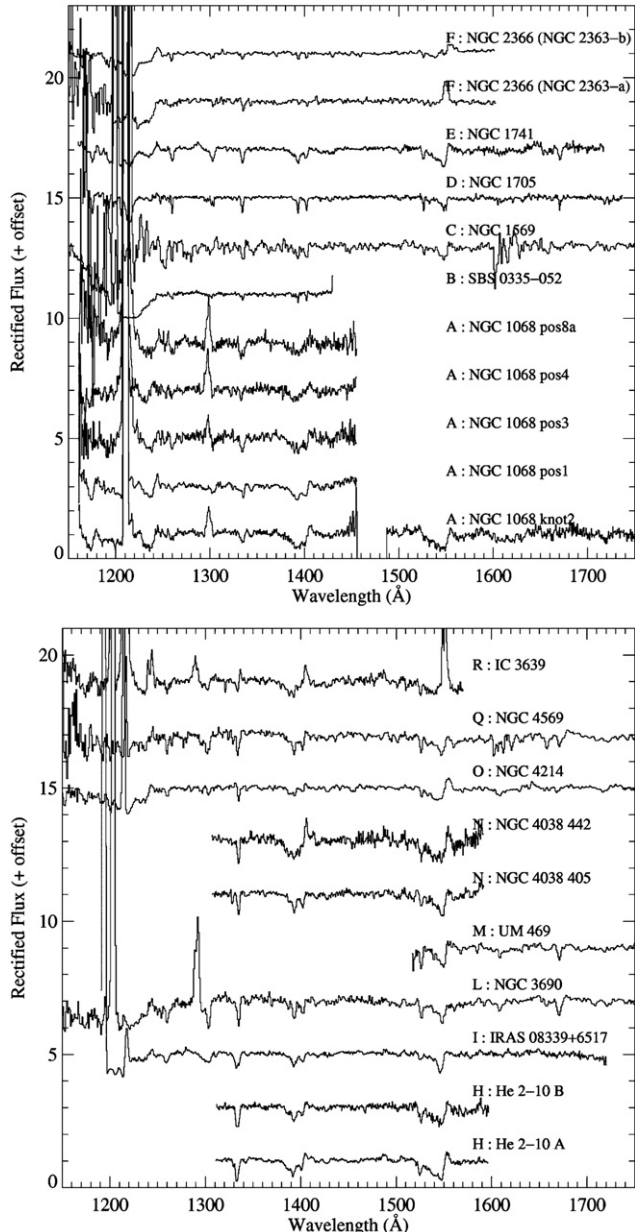


Figure 3. Galaxies with spectra in the 1150–1750 Å region arranged by right ascension. Spectra are labeled with a capital letter followed by the name of the galaxy. The capital letter preceding the galaxy name is the identifier introduced in Table 2. The intervening Milky Way ISM lines have been subtracted from the spectra as described in Section 3.5. The Ly α and O I $\lambda 1304$ airglow lines have not been removed from the spectra. Details about the individual observations can be found in Table 2.

in most cases. The O I emission is about a factor of 100 fainter; however, so we made measurements of starburst absorption features in the vicinity (typically the O I and Si II lines), but consider the airglow contamination as a possible (large) source of error.

3.6. The Spectral Atlas

The final corrected spectra are presented in Figure 3–Figure 6. The spectral coverage for the majority of the starburst region is incomplete and in many cases confined to shorter wavelengths. In Figure 3, we reproduced those galaxies with available spectra between 1150 and 1750 Å. These spectra were taken the G130H and G140L gratings of FOS and GHRS, respectively. Those

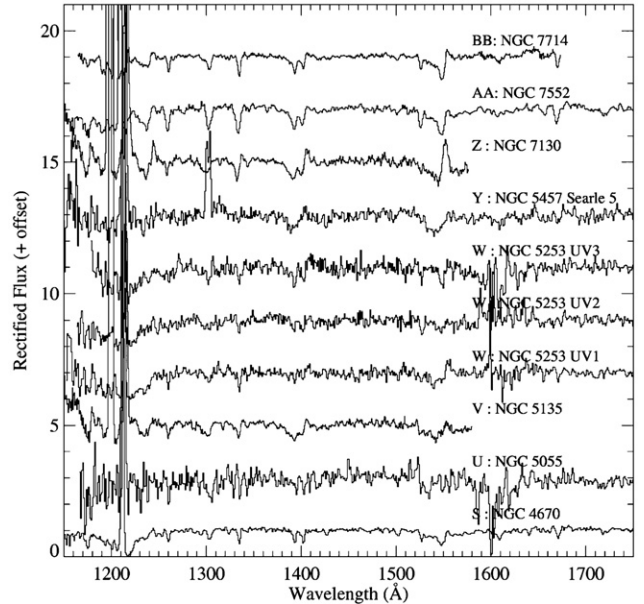


Figure 3. (Continued)

galaxies with spectra in the 1700–2300 Å region are shown in Figure 4. The FOS and its G190H grating were used in all cases. Relatively few galaxies were observed at the longest wavelengths in the 2300–3200 Å region (Figure 5). This wavelength region contains few stellar lines in young starbursts and has received less attention than the line-rich regime at shorter wavelengths.

We generated panchromatic spectra covering the entire 1150–3200 Å for the seven starburst regions with full spectral coverage. The spectra for these galaxies were obtained with the G130H, G190H, and G270H gratings of FOS. They are reproduced in Figure 6. Finally, we constructed a composite starburst spectrum by taking the median of all available spectra at each wavelength. A continuum normalized version of this spectrum is shown in Figure 7. This spectrum is particularly useful for comparison with spectra of star-forming galaxies. It provides guidance for the expected stellar and interstellar lines over the wavelength region 1175–3000 Å and can be used, e.g., as a template for isolating the massive star component in a galaxy with mixed populations. In order to study the influence of metallicity on the spectra, we constructed separate high- and low-metallicity templates. The high-metallicity template was restricted to galaxies with $12 + \log(\text{O/H}) > 8.7$, and the low-metallicity template to $12 + \log(\text{O/H}) < 8.2$. These two templates are contrasted in Figure 8. As expected, the spectral features are generally weaker at lower metallicity. The stellar-wind lines (e.g., C IV $\lambda 1550$) are not only weaker at lower metallicity but also show a smaller blueshift. This is the result of stellar winds having lower terminal velocities at lower metal abundance.

All spectral templates are available in electronic format from <http://www.stsci.edu/science/starburst/templ.html>. We provide two versions of the fully processed spectra: (1) spectra in the observed frame and (2) spectra in the galaxy rest frame with corrections applied for the dust obscuration and ISM line absorption caused by the Milky Way.

4. MULTI-WAVELENGTH GALAXY PROPERTIES

The principal advantage of using a sample composed of well-studied nearby galaxies is the existence of a large body

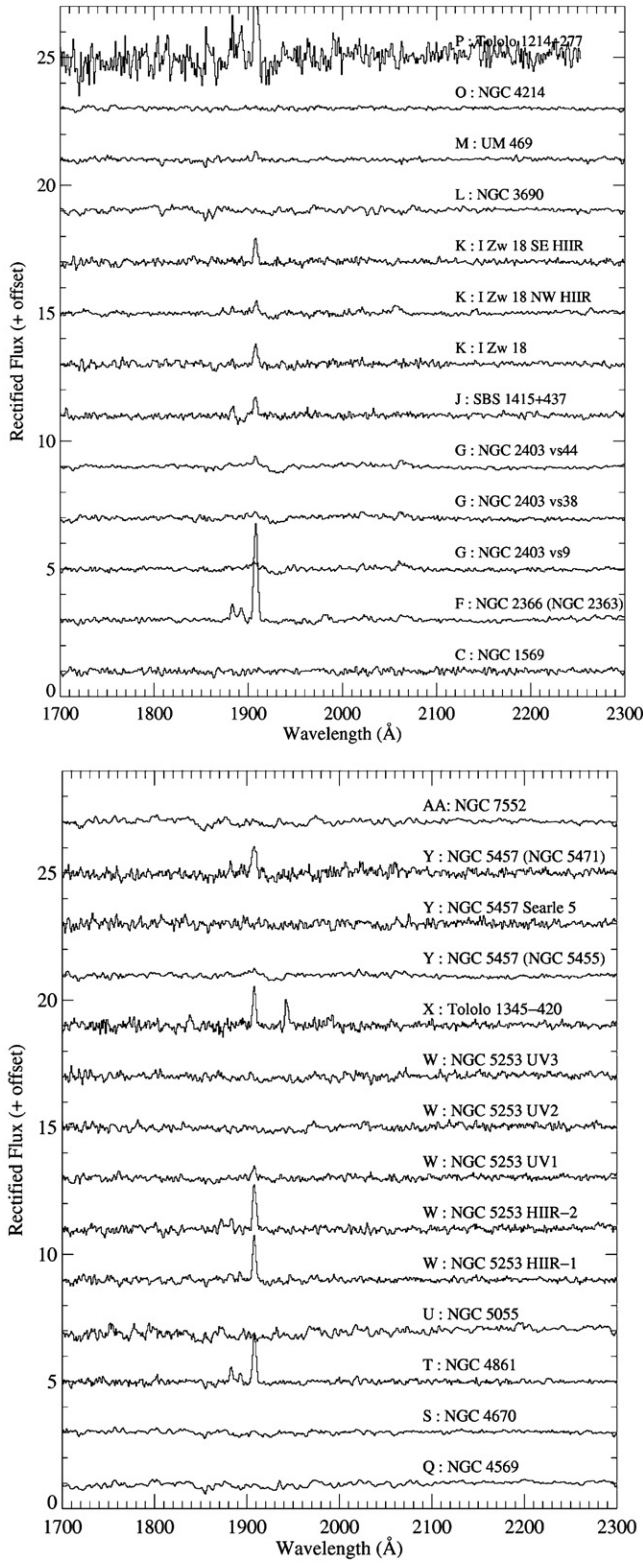


Figure 4. Galaxies with spectra in the 1700–2300 Å region. All of these spectra were obtained with the FOS and the G190H grating. They have been corrected for foreground Milky Way ISM line contamination as described in Section 3.5. The emission features are the nebular lines Si III $\lambda\lambda$ 1882/92 and C III] $\lambda\lambda$ 1907/09.

of multi-wavelength data in the literature. We use these data to obtain measures of the galaxy physical properties such as mass, metallicity, and starburst luminosity. In Table 4, we record a number of relevant quantities. Except for

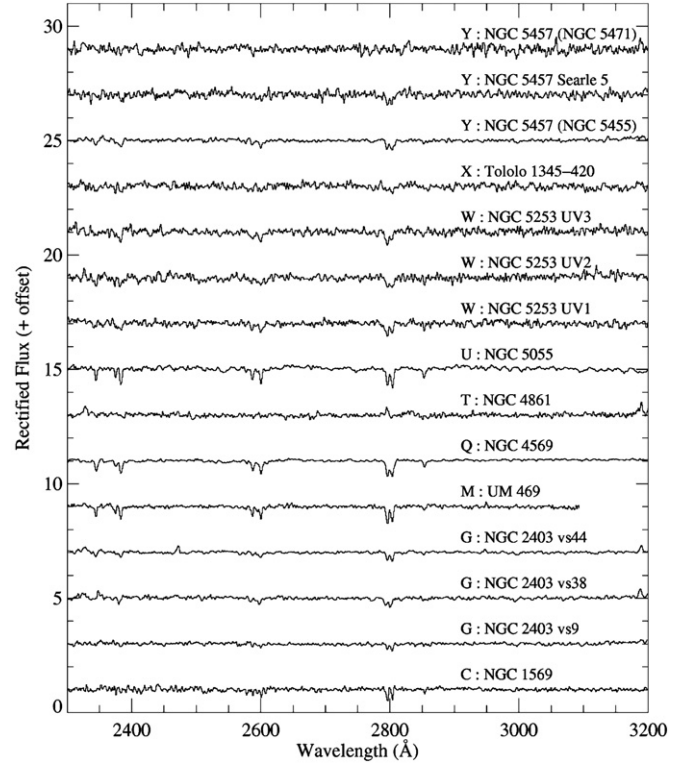


Figure 5. Galaxies with spectra in the 2300–3200 Å region. All of these spectra were obtained with the FOS and the G270H grating. They have been corrected for foreground Milky Way ISM line contamination as described in Section 3.5.

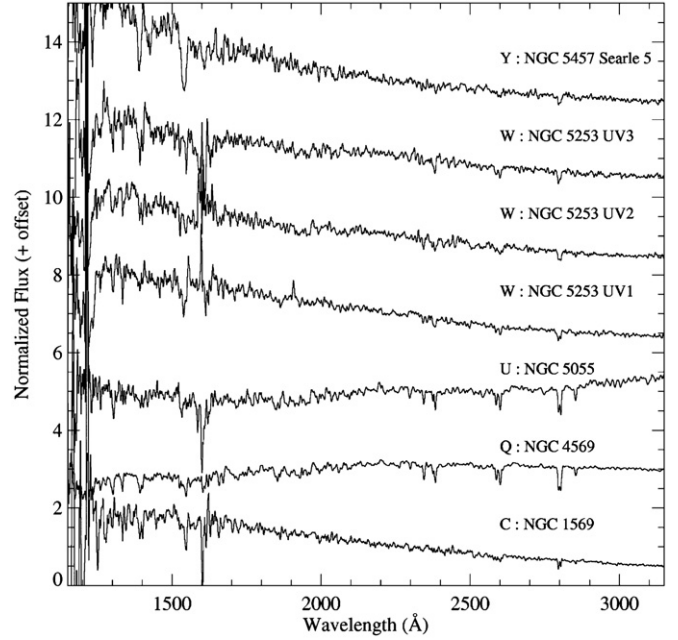


Figure 6. Galaxies with spectra covering 1150–3200 Å. These spectra were obtained with the FOS G130H, G190H, and G270H gratings and subsequently combined. (Note the relatively noisy join region around 1600 Å.) The spectra have been corrected for foreground Milky Way ISM line contamination and reddening as described in Section 3.5. The spectra have been normalized by their median flux, offset from one another, and smoothed by 5 pixels for clarity.

the properties noted further below, these quantities were obtained from the NASA/IPAC Extragalactic Database (NED): galaxy morphology (Column 2), heliocentric velocity v_{helio} (Column 3), blue magnitude m_B (Column 4), optical diameter

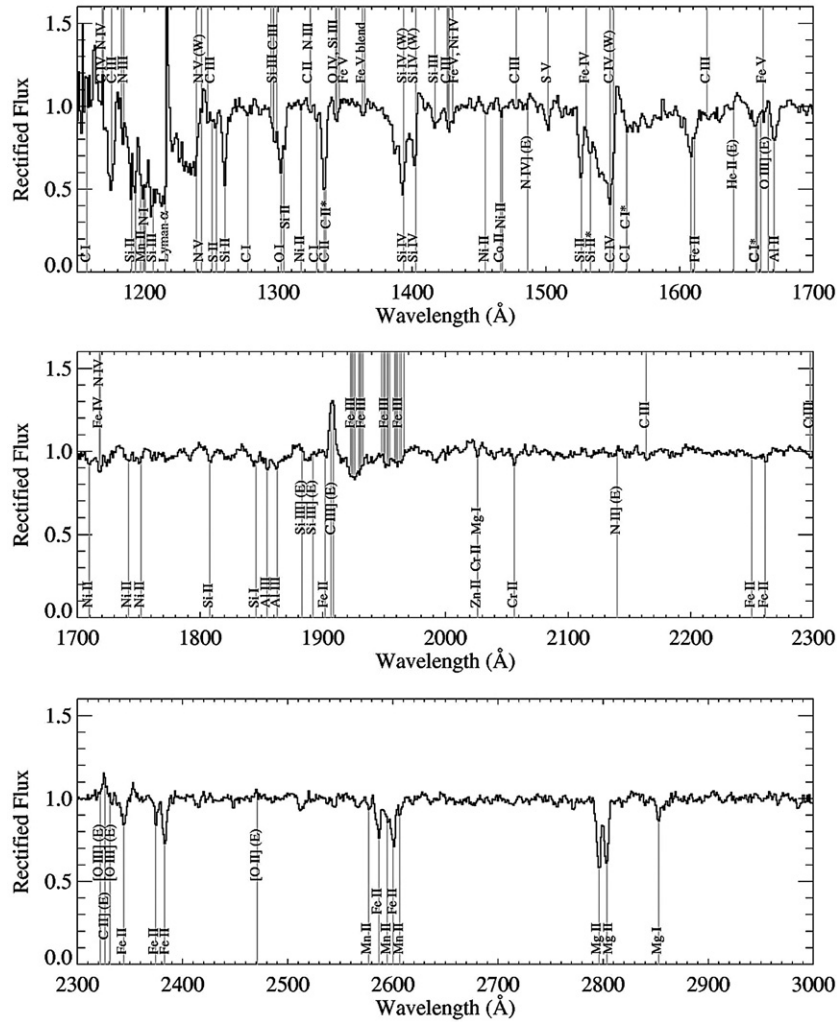


Figure 7. Composite starburst spectrum constructed from our sample spectra by taking the median of the available spectra at each wavelength. Prominent interstellar lines are labeled below the spectrum; stellar-wind and photospheric features are labeled above. The stellar-wind lines are denoted with a “W.” Nebular emission lines are signified with an “E.” Laboratory wavelengths for the marked features can be found in Table 1.

D_{optical} (Column 5), inclination i (Column 6), foreground reddening $E(B-V)$ (Column 7), and a list of alternate names (Column 8). The blue magnitudes have been taken preferentially from the RC3.9 catalog (de Vaucouleurs et al. 1991) and alternately from the ESOLV catalog (Lauberts & Valentijn 1989). Except in a minority of cases, the RC3 magnitudes are B_T magnitudes, which have not been k -corrected or corrected for Galactic extinction. The galaxy inclinations are from Huchtmeyer & Richter (1989). The values of $E(B-V)$ tabulated come from Schlegel et al. (1998), with the exception of the values listed for NGC 1569 and I Zw 18, which come from *HST* photometry (Angeretti et al. 2005; Aloisi et al. 2007).

In Table 5, we collate infrared (IR), UV, and H α data for our sample. The *IRAS* 60 and 100 μm fluxes (Columns 2 and 3 of this table) were taken preferentially from the catalog of *IRAS* observations of large optical galaxies by Rice et al. (1988), then from the *IRAS* Bright Galaxy Sample (Soifer et al. 1989) and from the *IRAS* Faint Source Catalog (Moshir et al. 1993). The *IRAS* fluxes for He 2–10 are from the *IRAS* Point Source Catalog (Beichman et al. 1988).

We measured UV fluxes directly from the *IUE* spectra in two 100 Å bandpasses defined by Kinney et al. (1993) beginning at 1432 and 1863 Å. Reduced spectra were obtained in electronic form from the Kinney et al. atlas where possible. The

remaining spectra were downloaded in processed form from the *IUE* archive. We combined all available *IUE* archive spectra with reasonable S/N obtained through the large ($10'' \times 20''$) aperture at the same pointing, including data from the Short Wavelength camera (SWP; 1150–2000 Å; $\Delta\lambda \approx 5$ Å) and the Long Wavelength cameras (LWR and LWP; 1900–3300 Å; $\Delta\lambda \approx 8$ Å). Before measuring the fluxes, the spectra were corrected for foreground Galactic extinction and deredshifted. The fluxes recorded in Columns 4 and 5 of Table 5 are the average fluxes in each bandpass. For each of the *IUE* spectra we also measured the spectral slope, β_{IUE} (Column 6), using a method similar to that of Calzetti et al. (1994).

$\text{H}\alpha$ data were used to derive the parameter Δv_{20} , which represents the measured width of the galaxy's $\text{H}\alpha \lambda 21\text{ cm}$ emission line at 20% of the peak intensity (Column 7). When corrected for inclination, Δv_{20} is approximately twice the galaxy rotation speed and hence is a good proxy for mass. The values in Column 7 are not corrected for inclination. The corrected values are in Table 6 (see below). The $\text{H}\alpha$ data were taken from the sources listed in Column 8. In cases where multiple measurements were listed, we chose the observation with the largest beam size to obtain the fullest sampling of the galaxy rotation curve.

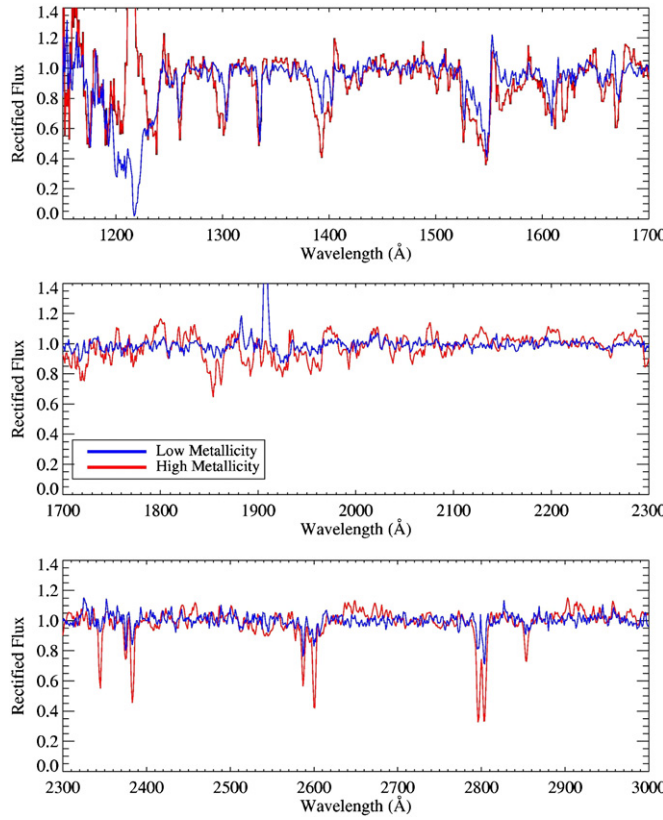


Figure 8. Similar to Figure 7, but for two subsets of galaxy spectra: a high-metallicity set with $12 + \log(\text{O/H}) > 8.7$ (red) and a low-metallicity set with $12 + \log(\text{O/H}) < 8.2$ (blue).

(A color version of this figure is available in the online journal.)

Column 9 of Table 5 gives the K magnitudes (m_K) for the galaxy sample. The values were taken from the sources in Column 10. The *Galaxy Evolution Explorer (GALEX)* far-UV magnitudes (m_{FUV}) are in Column 11. The *GALEX* far-UV channel covers the wavelength region from ~ 1350 to 1750 Å, with peak sensitivity around 1500 Å. The magnitudes were taken from Gil de Paz et al. (2007). β_{GALEX} in Column 12 is the UV spectral slope calculated from the *GALEX* FUV and NUV fluxes listed by Gil de Paz et al.

In Table 6, we list a variety of physical parameters of the galaxy sample. The galaxy distances d are in Column 2. We used direct distances where available from the *HST* key project and from various *HST* programs where the tip of the red giant branch was measured. The remaining distances are taken from the NASA/IPAC Extragalactic Database (NED). They were computed from the galaxy redshift assuming $H_0 = 73$ km s $^{-1}$, $\Omega_{\text{matter}} = 0.27$, $\Omega_{\text{vacuum}} = 0.73$ (Spergel et al. 2007) and using a model for the local Hubble flow that includes the Virgo Cluster, the Great Attractor, and the Shapley Supercluster (Mould et al. 2000). The reference for each galaxy is in Column 3.

We derived absolute B magnitudes (M_B ; Column 4) from the apparent magnitudes in Table 4 and the distances given in Column 2 of Table 6. We corrected for foreground extinction, but not for any extinction internal to the galaxy. We have not applied k -corrections since these would be negligible, given the low redshift of our sample. Likewise, we derived absolute K magnitudes (M_K ; Column 5) from the apparent magnitudes in Table 5. In the analysis that follows, we will use M_K to characterize the starburst host galaxy. One concern is that the light from the starburst itself might contribute significantly

to M_K . However, this was shown not to be the case for M_B in the H98 sample, which is similar in character to the present one. H98 calculated that the median contribution of the starburst to the total B -band galaxy light was only 20% in the absence of dust extinction. We will assume that the same applies to the K band and that the K -band luminosity is dominated by the luminosity of the host galaxy.

The UV and IR luminosities L_{UV} and L_{IR} reported in Columns 6 and 7 of Table 6, respectively, are expected to arise primarily from the young stellar population in the starbursts. We derived an estimate of the total UV luminosity between 912 and 3650 Å using the relation

$$\log L_{\text{UV}} = \log L_{1500} + 3.2,$$

where L_{UV} is in erg s $^{-1}$ and L_{1500} is in erg s $^{-1}$ Å $^{-1}$ (Leitherer et al. 2002). The UV luminosity we tabulate is corrected for Galactic foreground extinction, but not for extinction internal to the starburst. For the case of an unreddened starburst, the adopted definition of L_{UV} would include about 75% of the bolometric luminosity of the starburst, assuming no underlying old population (Leitherer et al. 2002). We approximated L_{1500} using the *GALEX* far-UV fluxes (Column 11 of Table 5) when available. For those galaxies without *GALEX* data we used the average *IUE* fluxes in the 1432–1532 Å interval (recorded in Column 4 of Table 5). Since our aim is to tabulate the global properties of the galaxies, the *GALEX* flux is a better measure of the starburst luminosity than the *IUE* flux because the *GALEX* field of view encompasses the entire galaxy. One practical concern is that a fraction of the UV flux will be missing in those cases without *GALEX* data. We can estimate the fraction of the UV flux not included in the *IUE* data by comparing L_{1500} for those galaxies with both *IUE* and *GALEX* data available. On average, L_{1500} derived from *IUE* is $\sim 25\%$ of the *GALEX* value. While this is significant, our main conclusions are not primarily dependent on L_{1500} , but rather on the total bolometric luminosity, which is the sum of $L_{\text{UV}} + L_{\text{IR}}$ as discussed in the following paragraph. In most cases, the L_{IR} is the dominant term. Moreover, the relations shown in the figures extend over 2–3 orders of magnitude in luminosity, which is much larger than a potential 0.6 dex offset in L_{1500} .

We calculated the total far-IR flux F_{IR} from the *IRAS* 60 and 100 μm fluxes according to the prescription of Helou et al. (1988):

$$F_{\text{IR}} = 1.26(2.58 f_{60} + f_{100})10^{-11} \text{ erg s}^{-1} \text{ cm}^{-2}.$$

The L_{IR} values listed in Column 7 of Table 6 were obtained from F_{IR} and the distances in Column 2. The sum of the UV and IR luminosities approximates the intrinsic UV luminosity since the IR emission is primarily powered by UV photons which have been absorbed and re-radiated by dust grains (Meurer et al. 1999; Leitherer et al. 2002; Calzetti 2008). Consequently, the ratio of $L_{\text{UV}}/L_{\text{IR}}$ is a good measure of the dust content.

The width of the $\text{H}\alpha \lambda 21$ cm line (Column 8 of Table 6) characterizes the host galaxy (rather than the starburst). In the simple case of circular rotation, this value is related to the line-of-sight rotation speed. The values reported in the table have been corrected for galaxy inclination (see Table 4) where possible. Under the assumption that the $\text{H}\alpha$ line width traces the rotation speed, $\Delta v_{20,i}$ is a good proxy for galaxy mass. However, it is likely that turbulent motions contribute or even dominate for galaxies which have experienced recent mergers (e.g., IRAS 0833+6517) and for some of the dwarfs.

Table 4
Optical Properties of the Galaxies

Galaxy	Morphology	v_{helio} (km s $^{-1}$)	m_B	D_{optical} (arcminute)	i (deg)	$E(B - V)$	Other Names
NGC1068	(R)SA(rs)b; Sey2	1137	9.6	7.1×6.0	40	0.03	M77, UGC 02188, IRAS 02401–0013, Arp 037
SBS0335–052	BCG	4043	16.6	0.23×0.20	...	0.05	SBS 0335–052E
NGC1569	IBm	−104	11.9	3.6×1.8	63	0.55	UGC 03056, ARP 210, VII Zw 016, IRAS 04260+6444
NGC1705	SAO–pec, HII	628	12.8	1.9×1.4	78	0.01	ESO158-G 013, IRAS 04531–5326
NGC1741	SB(s)m pec, HII	4107	13.3	0.61×0.23	62	0.05	MRK 1089, ARP 259, IRAS 04591–0419
NGC2366	IB(s)m	100	11.4	8.1×3.3	62	0.04	UGC 03851, IRAS 07233+6917
NGC2403	SAB(s)cd, HII	131	8.9	21.9×12.3	57	0.04	UGC 03918, IRAS 07321+6543
He2–10	I0 pec	873	12.4	1.93×1.35	32	0.11	ESO 495-G 021, IRAS 08341–2614
IRAS08339+6517	Pec HII	5730	14.2	0.3×0.3	...	0.09	PGC 024283
SBS1415+437	BCG	609	15.6	0.75×0.15	...	0.01	CGCG 219–066, CG 0389
I Zw 18	Compact	751	16.1	0.3×0.1	57	0.04	MKN 116, UGCA 116, SBS 0930+554
NGC3690	Ibm pec+Sbm Pair, HII	3121	12.0	2.0×1.5	42	0.02	MRK 0171, IRAS 11257+5850, ARP 299
UM 469	HII	17388	18.0	0.29×0.15	...	0.03	IRAS F11546+0245, Tololo 1154+027
NGC4038	SB(s)m pec	1642	10.9	5.2×3.1	51	0.05	UGCA 264, ESO 572-IG 047, ARP 244, Antennae
NGC4214	IAB(s)m, HII	291	10.2	8.5×6.6	37	0.02	NGC 4228, UGC 07278, IRAS 12131+3636
Tololo1214–277	HII	7795	17.5	0.08×0.08	...	0.06	Tololo 21, SCHG 1214–277
NGC4569	SAB(rs) ab, LINER	−235	10.3	9.5×4.4	63	0.05	M90, UGC 07786, ARP 076, IRAS 12343+1326
IC3639	Sb(rs)bc, Sey2	3275	13.0	1.2×1.2	...	0.07	ESO 381-G08, Fairall 0312, IRAS 12381–3638, Tololo 74
NGC4670	SB(s)o/a pec, BCDG	1069	13.1	1.4×1.1	37	0.01	UGC 07930, ARP 163, HARO9, IRAS 12428+2724
NGC4861	SB(s)m	847	12.9	4.0×1.5	67	0.01	IC 3961, UGC 08098, ARP 266, I Zw 049, MRK 59
NGC5055	SA(rs)bc, HII, LINER	504	9.3	12.6×7.2	55	0.02	M63, UGC 08334, IRAS 13135+4217, Sunflower
NGC5135	SB(l)ab, Sey2	4112	12.9	2.6×1.8	67	0.06	ESO 444-G 032, Tololo 34, IRAS 13229–2934
NGC5253	Im pec, HII	404	11.2	5.0×1.9	77	0.06	UGC 369, ESO 445-G 004, Haro 10, IRAS 13370–3123
Tololo1345–420	HII	2398	16.3	0.22×0.18	...	0.10	Tololo 111, SCHG 1345–421
NGC5457	SAB(rs)cd	241	8.3	28.8×26.9	24	0.01	M101, UGC 08981, ARP 026, IRAS 14013+5435
NGC7130	Sa pec, LINER	4842	12.9	1.5×1.4	25	0.03	IC 5135, ESO 403-G 032, IRAS 21453–3511
NGC7552	SA(s)c pec, HII, LINER	1585	11.2	3.4×2.7	46	0.01	IC 5294, ESO 291-G 012, IRAS 23134–4251
NGC7714	SB(s)b:pec, HII, LINER	2798	13.0	1.9×1.4	43	0.05	UGC 12699, ARP 284, MRK 538, IRAS 23336+0152

Table 5
Multi-wavelength Properties of the Galaxies

Galaxy	IRAS 60 μm	IRAS 100 μm	IUE 1500 Å	IUE 1900 Å	β_{IUE}	$\text{H}\alpha \Delta v_{20}$ (km s $^{-1}$)	Reference	M_K (mag)	Reference	m_{FUV} (mag)	β_{GALEX}
NGC1068	176.2	224.0	8.61	9.68	−0.57	298	1	5.79	5	12.52	−0.58
SBS0335–052	1.13	0.64	−2.19	105	2	15.63	6
NGC1569	45.4	47.3	72.69	47.29	−1.19	102	3	7.86	5	9.85	−0.44
NGC1705	1.0	2.6	17.95	8.98	−2.44	163	1	10.52	5
NGC1741	3.9	5.8	4.10	2.76	−1.55	217	1	11.84	7
NGC2366	3.5	4.7	7.30	5.71	−1.80	126	4	10.62	5	12.50	−1.69
NGC2403	51.5	148.5	0.59	0.35	−0.66	272	4	6.19	5	10.37	−1.44
He2–10	24.1	26.4	2.41	2.02	−0.68	156	1	9.00	7
IRAS08339+6517	5.9	6.5	7.43	4.76	−1.48	367	4	10.64	7
SBS1415+437	74	2
I Zw 18	2.10	1.15	−2.38	84	2	15.92	8	15.82	−1.98
NGC3690	103.7	107.4	2.65	1.90	−1.21	219	4	8.42	5
UM 469	0.3	0.6	15.06	6
NGC4038	48.7	82.0	408	4	7.18	5	12.82	−1.07
NGC4214	17.9	29.0	12.26	7.46	−1.74	82	1	7.91	5
Tololo1214–277
NGC4569	9.2	27.3	...	1.50	399	4	6.58	5	14.46	1.08	
IC3639	7.5	10.7	1.79	1.27	−0.91	9.69	7
NGC4670	2.6	4.5	7.18	4.58	−1.68	168	4	10.41	7
NGC4861	2.0	2.5	10.74	5.89	−2.48	116	4	11.77	5	13.54	−1.92
NGC5055	40.0	157.7	...	0.23	...	406	4	5.61	5	12.41	−0.68
NGC5135	16.9	28.6	1.51	1.85	−0.19	8.83	5
NGC5253	30.0	30.9	21.56	16.03	−1.42	96	1	8.25	5	12.20	−0.89
Tololo1345–420	14.11	7
NGC5457	88.0	252.8	1.10	0.80	−1.17	210	4	5.51	5	9.98	−1.49
NGC7130	16.5	25.6	1.07	0.84	−0.20	9.20	7
NGC7552	72.0	101.5	1.92	2.12	0.40	366	4	7.54	5	14.18	−0.20
NGC7714	10.4	11.5	5.49	3.75	−1.24	264	4	9.76	5

Note. IRAS fluxes are in Jansky and IUE fluxes are in 10^{-14} erg s $^{-1}$ cm $^{-2}$ Å $^{-1}$.

References. (1) Kobulnicky & Gebhardt 2000; (2) Thuan et al. 1999; (3) Meurer et al. 1998; (4) Huchtmeier & Richter 1989; (5) Jarrett et al. 2003; (6) Two Micron All Sky Survey (2MASS) Point Source Catalog; (7) 2MASS Extended Source Catalog; (8) Thuan 1983.

Table 6
Physical Properties of the Galaxies

Galaxy	<i>d</i> (Mpc)	Reference	<i>M_B</i> (mag)	<i>M_K</i> (mag)	$\log L_{\text{UV}}$	$\log L_{\text{IR}}$	$\text{H}\alpha \Delta v_{20,i}$ (km s ⁻¹)	12+log(O/H)	Reference	<i>A_{IUE}</i> (pc)	<i>A_{HST}</i> (pc)
NGC 1068 knot2	15.2	1	-21.4	-25.1	43.3	44.4	463	9.2	12	1105	147
NGC 1068 pos1								9.1	12	1105	128
NGC 1068 pos3								9.1	12	1105	128
NGC 1068 pos4								9.1	12	1105	128
NGC 1068 pos8a								9.1	12	1105	128
SBS 0335-052	53.7	1	-17.1	-18.0	42.8	...	105	7.3	13	3905	452
NGC 1569	2.2	2	-16.6	-18.9	42.7	42.1	114	8.2	14	159	2
NGC 1705	5.1	3	-15.8	-18.0	41.9	41.3	166	8.2	15	370	5
NGC 1741	54.6	1	-20.5	-21.8	43.4	43.9	245	8.1	16	3970	460
NGC 2366 (NGC 2363)	3.4	4	-16.4	-17.1	42.0	41.4	142	7.9	17	250	16
NGC 2366 (NGC 2363-a)								7.9	17	250	14
NGC 2366 (NGC 2363-b)								7.9	17	250	14
NGC 2403 vs9	3.1	5	-18.7	-21.3	42.8	42.6	324	8.1	18	225	12
NGC 2403 vs38								8.5	18	225	12
NGC 2403 vs44								8.5	18	225	12
He 2-10 A	10.4	1	-18.0	-21.1	41.7	43.2	294	8.9	19	756	87
He 2-10 B								8.9	19	756	87
IRAS 08339+6517	81.5	1	-20.7	-23.9	44.0	44.3	367	8.4	20	5926	687
SBS 1415+437	13.6	6	-15.1	74	7.4	13	...	56
I Zw 18	18.2	7	-15.3	-15.4	42.1	...	100	7.2	13	1323	88
I Zw 18 NW HII R								7.2	13	1323	75
I Zw 18 SE HII R								7.3	13	1323	75
NGC 3690	48.5	1	-21.5	-25.0	43.1	45.1	327	8.8	21	3527	235
UM 469	246.1	1	-19.1	-21.9	...	44.1	...	8.0	13	...	1026
NGC 4038 405	22.0	8	-21.0	-24.5	43.5	44.2	524	9.1	22	...	185
NGC 4038 442								9.1	22	...	185
NGC 4214	2.9	9	-17.2	-19.4	41.3	42.0	136	8.1	19	213	14
Tololo 1214-277	115.6	1	-18.0	7.5	13	...	560
NGC 4569	9.0	10	-19.7	-23.2	42.1	42.8	447	37
IC 3639	35.3	1	-19.9	-23.0	42.6	43.8	2567	297
NGC 4670	23.1	1	-18.8	-21.4	42.9	43.0	279	8.2	21	1679	111
NGC 4861	15.0	1	-18.0	-19.1	42.9	42.4	126	7.9	13	1090	62
NGC 5055	8.7	1	-20.5	-24.1	42.9	43.5	495	9.0	12	...	36
NGC 5135	57.7	1	-21.1	-25.0	43.0	44.6	4196	486
NGC 5253 HII R-1	3.6	5	-16.8	-19.5	42.2	42.3	98	8.2	23	261	15
NGC 5253 HII R-2								8.2	23	261	15
NGC 5253 UV1								8.3	23	261	15
NGC 5253 UV2								8.3	23	261	15
NGC 5253 UV3								8.3	23	261	15
Tololo 1345-420	26.1	1	-16.1	-18.0	8.0	13	...	108
NGC 5457 (NGC 5455)	7.4	11	-21.1	-23.8	43.7	43.6	516	8.2	24	536	30
NGC 5457 Searle 5								8.6	24	536	35
NGC 5457 (NGC 5471)								8.0	24	536	30
NGC 7130	68.7	1	-21.4	-25.0	43.0	44.7	4996	579
NGC 7552	22.5	1	-20.6	-24.2	43.0	44.3	508	9.2	21	1636	109
NGC 7714	38.5	1	-20.1	-23.2	43.2	43.9	387	8.5	25	2799	324

References. (1) NASA Extragalactic Database (NED); (2) Angeretti et al. 2005; (3) Tosi et al. 2001; (4) Karachentsev et al. 2003; (5) Sakai et al. 2004; (6) Aloisi et al. 2005; (7) Aloisi et al. 2007; (8) Schweizer et al. 2008; (9) Maíz-Apellániz et al. 2002; (10) Shapley et al. 2001; (11) Ferrarese et al. 2000; (12) Garnett 2002; (13) Nava et al. 2006; (14) Kobulnicky & Skillman 1997; (15) Lee & Skillman 2004; (16) Izotov et al. 2007; (17) Esteban et al. 2002; (18) Garnett et al. 1997; (19) Kobulnicky et al. 1999; (20) López-Sánchez et al. 2006; (21) H98; (22) Bastian et al. 2006; (23) López-Sánchez et al. 2007; (24) Kennicutt et al. 2003; (25) González-Delgado et al. 1995.

The nebular oxygen abundances of the galaxies are listed in Column 9 of Table 6. In the case of multiple pointings with available oxygen abundances, we list the values for all pointings but give the other properties for the first pointing only. The solar oxygen abundance in these units is 8.70 (Meléndez & Asplund 2008); Large Magellanic Cloud and Small Magellanic Cloud abundances are 8.4 and 8.0, respectively (Garnett 1999). The oxygen abundances quoted were obtained from a large number of sources. When several measurements were available, the most recent one was, in general, adopted. For a few of the most metal-poor systems, the oxygen abundance was calculated directly after measuring the electron tempera-

ture from the ratio of [O III] $\lambda 4363$ /[O III] $\lambda\lambda 4959, 5007$. However, for the majority of the galaxies, the abundance was computed using “strong-line methods,” which rely on empirical calibrations of various nebular line ratios such as, e.g., $([\text{O II}] + [\text{O III}])/\text{H}\beta$. The errors in this process can be large due to the necessity of removing the underlying Balmer absorption and correcting for reddening. Further systematic errors result from the disagreement among strong-line calibrations (Kewley & Ellison 2008). Moustakas et al. (2010) compared the oxygen abundances resulting from theoretical and empirical (strong-line) calibrations and found differences of a factor of ~ 5 . The sample of Moustakas et al. includes three galaxies studied in

this work: NGC 1705, NGC 2403, and NGC 5055. Their quoted theoretical and empirical oxygen abundances for these three galaxies are 8.3 and 8.0, 8.9 and 8.4, and 9.2 and 8.5, respectively. These values bracket our derived abundances listed in Table 6 and suggest that the errors in our tabulated abundance measurements are on the order of ± 0.3 dex. This is consistent with the spread in values seen when multiple measurements are available. H98 demonstrated that the metallicity of a starburst region has a pronounced impact on its UV spectrum. We have therefore obtained the metallicity closest to the actual *HST* pointing when possible. This is particularly important for spiral galaxies where there can be strong radial metallicity gradients of the order of 0.4 dex kpc $^{-1}$ (van Zee et al. 1998). Fortunately, the bright star clusters that *HST* observed were typically associated with bright giant H II regions where nebular metallicities were most likely to be obtained. Column 10 of Table 6 gives the references of the oxygen abundances.

5. STARBURSTS VERSUS STAR CLUSTERS: COMPARING *HST* AND *IUE*

An important goal of this work is to determine how much can be reliably deduced about a galaxy's physical properties based on its UV spectrum alone. H98 demonstrated that the strength of the stellar and interstellar lines and the spectral slope β measured in *IUE* data were strongly correlated with the global properties of the host galaxy. These correlations can be investigated in more detail with our higher quality *HST* data set, with the caveat that the *HST* apertures sample only a small part of the starburst. Since this is rather different from the situation at high redshift where the integrated light of the whole galaxy is observed, it is extremely important to investigate whether *HST* spectra are representative of the starburst properties as a whole.

The availability of *IUE* data for nearly all of our sample galaxies makes it possible to compare the UV properties of starbursts on two very interesting spatial scales. In Columns 11 and 12 of Table 6 we list the projected aperture sizes A_{IUE} and A_{HST} for each data set, respectively. The 10'' \times 20'' *IUE* aperture is a good match to the circumnuclear sizes (a few kpc) of most of the starbursts in our sample and the sizes of bright star-forming complexes (a few 100 pc) in the disks of nearby spirals. In contrast, the *HST* apertures (typically the 1''.74 Large Science Aperture for GHRS and the 0''.86 circular aperture for the FOS) generally encompass only a few bright star clusters. However, in starburst galaxies, one or a few bright clusters can account for a substantial portion of the UV light.

In Figure 9, we contrast the average UV fluxes of the *IUE* and *HST* spectra in the two bandpasses defined by Kinney et al. (1993). The median flux ratio is 15%; however, a few galaxies have over half of their UV flux in the *HST* aperture. This suggests that individual clusters can be important contributors to the total starburst luminosity but that star formation is typically more extended.

In the upper left panel of Figure 10, we compare the UV spectral slopes β_{IUE} and β_{HST} of the *IUE* and *HST* spectra, respectively. The values of β_{IUE} and β_{HST} have been measured using a method similar to that of Calzetti et al. (1994). Because the extent of the wavelength coverage can have a fairly strong effect on the measured spectral slope, we measure β_{IUE} and β_{HST} only over the wavelength region in common between the *IUE* and *HST* spectra to facilitate the comparison. (Note that because of the rather patchy nature of the *HST* wavelength coverage, the common wavelength region varies significantly from spectrum to spectrum.)

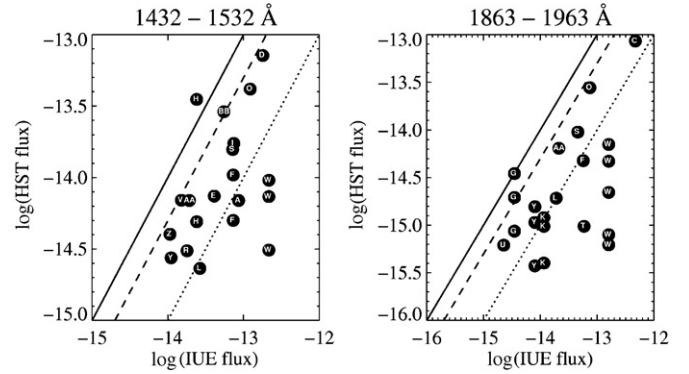


Figure 9. Comparison of the 1500 (left) and 1900 Å (right) fluxes measured in the *HST* and *IUE* apertures. Fluxes are in units of erg s $^{-1}$ cm $^{-2}$ Å $^{-1}$. The solid line is a one-to-one correlation; the dashed line a ten-to-one correlation. Individual galaxies are labeled by their identifiers defined in Table 2.

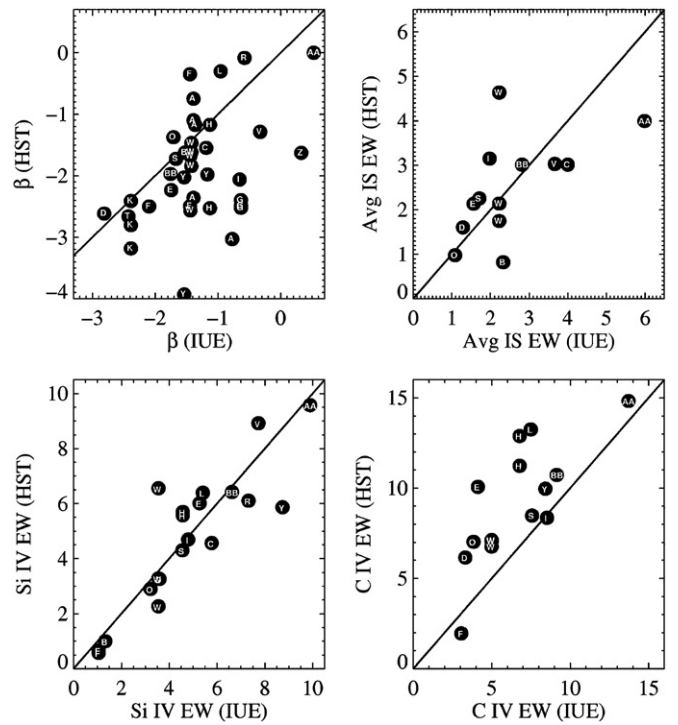


Figure 10. Upper left: comparison of the UV spectral slopes β_{HST} and β_{IUE} measured in the *HST* and *IUE* data, respectively. The *IUE* spectra have a spectral slope whose median is redder by 0.6. Upper right: absorption line EWs (Å) measured in the *HST* and *IUE* data. The label "Avg IS EW" denotes the average EW of the strongest interstellar features Si II λ1260, O I λ1303 + S II λ1304, and C II λ1335. Lower: EWs of the stellar-wind lines Si IV λ1400 (left) and C IV λ1550 (right). The solid line is a one-to-one correlation. Individual galaxies are labeled by their identifiers defined in Table 2.

Figure 10 suggests that the *IUE* spectra are redder on average than the *HST* spectra, with the median difference between β_{IUE} and β_{HST} being 0.6. This trend is likely to be partly a selection effect: in choosing targets for *HST* preference was usually given to the regions of the starburst with the highest UV surface brightness, thereby favoring clusters which were young but not heavily dust enshrouded. Another factor which could contribute to the color difference is the presence of underlying old stellar populations, which probably account for a larger fraction of the light in the *IUE* aperture, especially in cases where the starburst is fairly compact. It is of interest to determine if the difference in the UV spectral slopes in the *HST* and

IUE spectra can be accounted for purely by stellar population differences or whether some patchiness of the ISM is required. This has major implications for the “foreground screen” models of the dust distribution (Calzetti 2001) and for the leakage of ionizing photons into the intergalactic medium. Additional relevant clues can be provided by a comparison of the strong stellar and interstellar absorption lines as we will demonstrate in the following. Theoretical energy distributions predict $\beta \gtrsim -3$ (Leitherer et al. 1999). A few galaxies in Figure 10 fall outside this relation. However, we caution from over-interpreting this apparent discrepancy since all the outliers have limited spectral coverage and the measurement errors are large.

The UV spectral slopes in Figure 10 can also be compared to the slopes derived from the *GALEX* FUV and NUV fluxes β_{GALEX} (Column 12 in Table 5). Ten galaxies have available measurements of both β_{GALEX} and β_{IUE} . On average the two sets of UV spectral slopes agree: $\beta_{GALEX} - \beta_{IUE} = 0.02 \pm 0.57$. However, this agreement is significantly biased by several nearby, large galaxies such as NGC 2403 where aperture size effect comes into play. Most galaxies whose star formation is concentrated in nuclear star clusters have bluer *IUE* than *GALEX* slopes. This is consistent with the trend between *HST* and *IUE* suggested by Figure 10.

The upper right panel of Figure 10 compares the EW of the average of the three strongest interstellar absorption lines, Si II $\lambda 1260$, O I $\lambda 1303 +$ S II $\lambda 1304$, and C II $\lambda 1335$ measured in the *IUE* and *HST* spectra. For consistency, we have smoothed the *HST* data to the 6 Å resolution of *IUE* and used the windows defined by H98 to measure the EWs. ISM line EWs range from about 1 to 6 Å and appear to be in relatively good agreement with the *IUE* and *HST* spectra. Given that the apertures employed differ by roughly two orders of magnitude, this agreement is rather striking. Taken at face value, the results of this figure may suggest a constant covering factor when going from the small *HST* to the larger *IUE* apertures.

Although we cannot make use of the line profile information due to the low resolution of the *IUE* data (~ 1000 km s $^{-1}$), we can draw some inferences based on the ISM line EWs on the assumption that the lines are saturated. In this case, the EWs do not depend strongly on column density but reflect the velocity distribution and the covering factor of the gas. If rotation were the dominant factor affecting the line width, then pronounced differences would be expected between the small aperture *HST* observations and the large aperture *IUE* observations. The lack of such systematic differences in the measured EWs suggests a turbulent origin for the line widths. This is plausible given that starbursts deposit mechanical energy into the ISM via stellar winds and supernovae.

It is also illuminating to compare the EWs of the strong stellar-wind lines Si IV $\lambda 1400$ and C IV $\lambda 1550$. (Note that there is an interstellar contribution to the total EW as well.) We measured the stellar-wind lines in the same manner as the interstellar lines using the windows of H98. The lower two panels of Figure 10 show that the EW of Si IV is very similar in the *IUE* and *HST* spectra, while the EW of C IV is larger in the *HST* spectra by an average of 2.5 Å. The agreement of the Si IV lines and the disagreement of the C IV lines seem hard to reconcile at first since both features are a blend of interstellar absorption lines and stellar-wind P-Cygni features. One clue is the fact that the contribution of the wind lines to the absorption is greater at C IV than at Si IV. Using our same line measurement techniques on the Starburst99 models (Leitherer et al. 1999), we found that the difference in the EW of C IV at 5 Myr (when the wind lines are

maximal) and at 50 Myr (when the wind lines are absent and only interstellar lines contribute) is ~ 3 Å, whereas the difference for Si IV is only ~ 1 Å. The similarity between these numbers and the differences manifested in Figure 10 suggests this as the likely explanation, provided that the clusters observed by *HST* are younger than the surrounding starburst.

6. NEW MEASURES OF UV SPECTRAL FEATURES

In order to quantify the UV spectral morphology of galaxies, it is desirable to develop a repeatable method for measuring the various UV absorption features. The major challenge in this undertaking is fitting the UV continuum. The continuum is difficult to pinpoint—even by eye—due to the myriad weak stellar features, the strong absorption by Ly α , and the effects of reddening on the continuum shape. Most prior works utilized hand-tuned polynomial or power-law fits. We experimented with automated versions of these techniques with little success: power laws seemed to have trouble fitting the small-scale structure, while polynomials tended to fit too much structure and perform poorly at the endpoints. These techniques were also extremely sensitive to the wavelength coverage of the spectrum. It proved to be considerably more robust to define a local continuum for each spectral feature of interest.

To promote standardization, we have created a set of 12 UV line indices similar in form to the well-known Lick indices (Worley 1994; Schiavon 2007). These 12 indices are presented in Table 7. Column 1 of this table gives the name of the index. SiIV_1400 and CIV_1550 are the only indices which are typically dominated by stellar-wind lines. These indices are useful for determining ages, metallicities, and IMFs of stellar populations in star-forming galaxies (e.g., Leitherer 2010), in particular if the observational data have insufficient quality to permit detailed line profile fits. AlIII_1860 is a blend of wind and interstellar lines, and the remaining nine indices are mostly interstellar. As demonstrated by H98, the interstellar lines in starburst galaxies, even if saturated, are sensitive to the metallicity of the host galaxy and are therefore a useful abundance indicator. For each index we define a central bandpass and two flanking continuum bandpasses (Columns 2–4, respectively). We define the continuum at the midpoint of the flanking bands to be the median value of the flux within the bandpass. We use median rather than the average because it is more robust at low S/N levels and stable against spectral artifacts, such as the presence of a weak intervening absorber. The continuum in the central index bandpass is defined by a straight line connecting the midpoints of the two continuum bands. The most important stellar absorption features included in the bandpass of the index are in Column 5 of Table 7.

We have taken considerable care in placing both the central bandpass and the continuum bands. We have endeavored to make the central bandpasses broad enough to accommodate a range of velocity dispersions, but no broader than necessary. In several instances, we have grouped together several neighboring lines (e.g., Fe II_2370 = Fe II $\lambda 2344$, $\lambda 2374$, $\lambda 2383$). The continuum bands have been carefully chosen to avoid regions of stellar line blanketing, which show up clearly only in the most metal-rich systems. The indices are illustrated in Figure 11 and 12. The spectrum shown in Figure 11 is a high-metallicity composite made from the median of our sample galaxies with abundances greater than $12 + \log(O/H) = 8.7$ (see also Figure 8). The composite is illustrative because of its superior S/N and because the weak stellar features are strongest at high

Table 7
UV Line Indices

Index Name	Index Bandpass	Blue Continuum	Red Continuum	Features Included
SiII_1260	1255–1264	1268–1286	1268–1286	Si II 1260, Si II 1259
OI_SiII_1303	1290–1307	1268–1286	1308–1324	O I 1302, Si II 1304, Si III 1295
CII_1335	1326–1340	1308–1324	1348–1378	C II 1334, C II* 1335
SiIV_1400	1379–1405	1348–1378	1433–1460	Si IV 1393, 1402
SiII_1526	1521–1529	1460–1495	1572–1599	Si II 1526
CIV_1550	1529–1553	1460–1495	1583–1599	C IV 1548, 1550, Si II* 1533
FeII_1608	1600–1613	1583–1599	1614–1632	Fe II 1608
AlIII_1670	1663–1679	1614–1632	1680–1705	Al III 1670
AlIII_1860	1840–1873	1815–1839	1932–1948	Al III 1854, 1862
FeII_2370	2334–2391	2267–2290	2395–2450	Fe II 2344, 2374, 2382
FeII_2600	2578–2611	2525–2572	2613–2674	Mn II 2576, Fe II 2586, Mn II 2594, Fe II 2600, Mn II 2606
MgII_2800	2788–2810	2720–2785	2812–2842	Mg II 2796, 2803

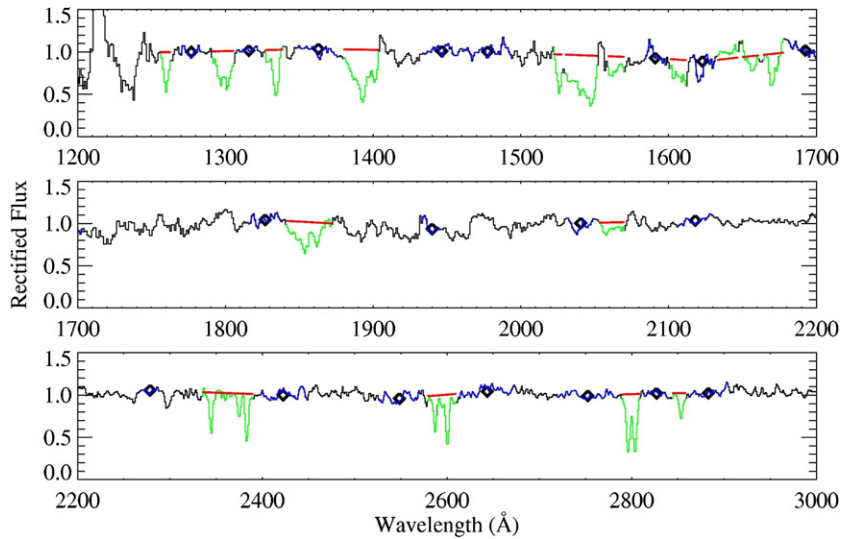


Figure 11. Composite high-metallicity spectrum with the positions of the UV line indices indicated. The continuum regions are shown in blue, with diamonds representing the average value of the bandpass. The central index bandpass is shown in green, with red lines illustrating the continuum.

(A color version of this figure is available in the online journal.)

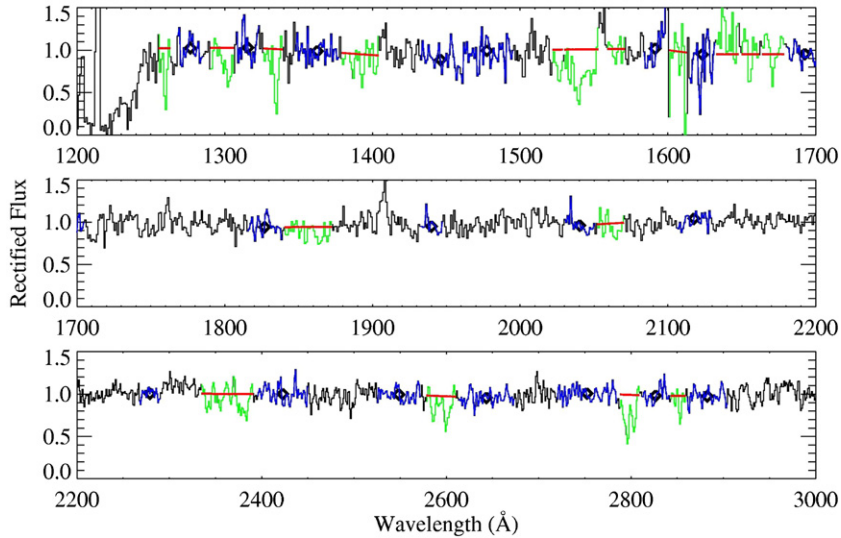


Figure 12. Example of a low S/N spectrum (NGC 5253-UV1) with the positions of the UV line indices indicated. The color coding is identical to that in Figure 11.

(A color version of this figure is available in the online journal.)

metallicity. In contrast, we show a relatively low S/N spectrum of NGC 5253 in Figure 12. This spectrum demonstrates that the indices do an adequate job of constraining the continuum even at modest S/N.

Following these definitions, we measured the line indices in all galaxy spectra where feasible. No measurements were performed in cases of active galactic nucleus activity leading to an emission contribution to the interstellar lines. The

measurements are summarized in Table 8. The table gives the line index measurements (in Å) in Columns 2–13, as well as the mean velocity of the nine interstellar indices with respect to the galaxy rest-frame velocity (Column 14).

We attempted to estimate the error in our index measurements even though we have not propagated the error array output by the *HST* pipeline through our final calibrations. We define the error in the continuum fit as the standard deviation of the data points in the blue and red bandpasses about the line defined as the continuum. This is appropriately propagated into the error in the EW of the index. A by-eye examination of the indices for our galaxies suggests that the predominant error source is the continuum fit. The method we have adopted of approximating the error in the line index appears to do a very good job of representing the general quality of our index measurements. We will use this method for the error estimates presented in the following section.

7. UV DIAGNOSTICS OF GALAXY PHYSICAL PROPERTIES

Having established that our *HST* spectra correlate with large-aperture UV spectra in predictable ways, we now turn to examining how the various spectral features in our *HST* data correlate with the physical properties of galaxies.

7.1. Correlations Between Starburst and Host Galaxy Properties

We are interested both in the properties of the starburst itself and those of the host galaxy. We characterize the starburst by its intrinsic UV luminosity $L_{\text{UV}} + L_{\text{IR}}$ and its dustiness—measured by the ratio of the emitted versus reprocessed flux $L_{\text{UV}}/L_{\text{IR}}$. The salient properties of the host galaxy are its luminosity (M_K), its mass (as traced by $\Delta v_{20,i}$), and its metallicity ($12 + \log(\text{O/H})$). As pointed out by H98 and many other authors, very strong correlations exist among the physical properties themselves: the most massive galaxies are the most optically luminous and metal-rich, and they host the dustiest and most UV-luminous starbursts. These correlations are shown for our sample in Figure 13. In this figure, we show how galaxy mass, metallicity, starburst strength, and dust obscuration correlate with the galaxy luminosity as expressed by M_K . Since mass, metallicity, dustiness, and host and starburst luminosity are all correlated with one another, we do not plot all possible combinations of parameters, but instead focus on the trends that are the most physically motivated.

We have included in some of the figures the well-studied lensed Lyman-break galaxies MS 1512-cB58 (Pettini et al. 2000), the “Cosmic Horseshoe” (Quider et al. 2009), and the “Eight O’clock Arc” (Dessauges-Zavadsky et al. 2010). The oxygen abundance of $\log(\text{O/H}) + 12 = 8.4$ of MS 1512-cB58 has been derived by Teplitz et al. (2000) based on IR observations of the common optical nebular emission lines and by Rix et al. (2004) from modeling weak photospheric absorption lines. Hainline et al. (2009) and Finkelstein et al. (2009) derived oxygen abundances of 8.4 and 8.6 using the N2 index for the Cosmic Horseshoe and the Eight O’clock Arc, respectively.

We have calculated the sum of the far-UV and far-IR luminosities for MS1512-cB58 using the rest-frame UV flux measured by Ellingson et al. (1996) and the rest-frame far-IR flux by Siana et al. (2008) assuming a gravitational lens amplification of 30 (Seitz et al. 1998). M_K was derived from the rest-frame

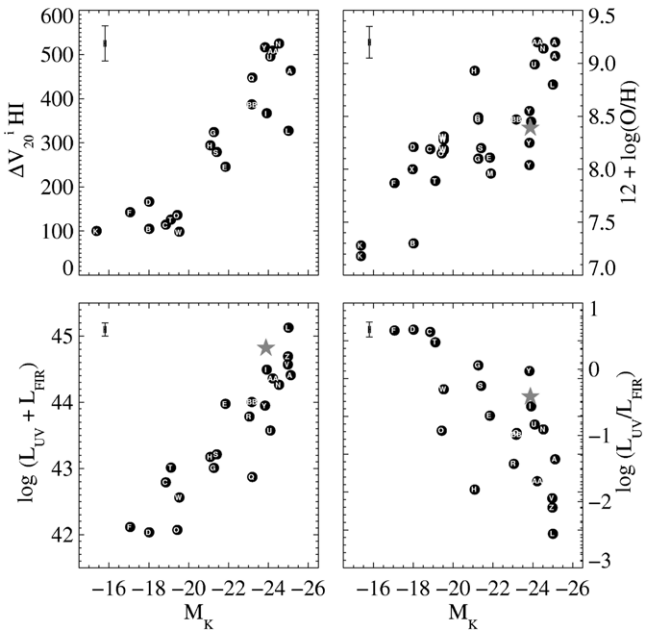


Figure 13. Correlations between galaxy luminosity M_K and other galaxy properties. Shown is clockwise starting from top left: mass, as traced by the width of the H I line, $\Delta v_{20,i}$; metallicity $12 + \log(\text{O/H})$; starburst strength $L_{\text{UV}} + L_{\text{IR}}$; dust obscuration $L_{\text{UV}}/L_{\text{IR}}$. The sample galaxies are represented with solid dots. The asterisk denotes the location of the Lyman-break galaxy MS 1512-cB58. Individual galaxies are labeled by their identifiers defined in Table 2.

$8 \mu\text{m}$ data in Siana et al. (2008). MS1512-cB58 clearly ranks among the most luminous starbursts and has correspondingly strong ISM features. There are no corresponding luminosity measurements for the other two Lyman-break galaxies.

7.2. Interstellar Lines: Correlations Between EW and Galaxy Parameters

We first discuss the interstellar lines. The UV interstellar lines hold great promise as diagnostics of high-redshift galaxy properties. The Si II $\lambda 1260$, O I $\lambda 1302 + \text{Si II } \lambda 1304$, and C II $\lambda 1335$ lines are some of the strongest features observed in UV starburst galaxy spectra, as shown by our composite spectrum in Figure 7. Previous studies of the ISM lines in starbursts have yielded important information about the chemical enrichment and gas kinematics of galaxies at both low and high redshift (Heckman & Leitherer 1997; Sahu 1998; Kunth et al. 1998; Pettini et al. 2002; Savaglio et al. 2004; Chen et al. 2007; Grimes et al. 2009). However, these works made use of high-resolution spectra which resolved the velocity structure of the ISM lines. Since such observations are costly in terms of telescope time, it is of interest to determine how much information can be reliably deduced from observations with moderate resolution.

We begin our analysis with a simple examination of the correlation of line EWs with the starburst luminosity and metallicity. We measured the interstellar absorption lines using the UV line indices defined in Section 6 and Table 7. The indices have been measured after subtracting off the foreground Milky Way ISM lines, as described in Section 3. The error in this correction has not been included in errors quoted for the line indices. Since we have endeavored to select continuum windows which are free of other features, our index measurements approximate true EWs and should therefore always be positive in the case of absorption (unlike the Lick indices which may take on positive or negative values due to changes in the continuum bands).

Table 8
Line Index Measurements

Galaxy	SiII_1260	OI_SiII_1303	CII_1335	SiIV_1400	SiII_1526	CIV_1550	FeII_1608	AlIII_1670	AlIII_1860	FeII_2370	FeII_2600	MgII_2800	v_{off} (km s $^{-1}$)
NGC 1068 knot2	1.05 ± 0.20	-3.43 ± 0.37	1.51 ± 0.25	9.07 ± 1.31	0.38 ± 1.60	10.41 ± 1.75	1.98 ± 0.46	-1.41 ± 0.79
NGC 1068 pos1	1.07 ± 0.14	2.60 ± 0.23	2.05 ± 0.22	8.28 ± 0.24
NGC 1068 pos3	2.01 ± 0.31	-1.21 ± 0.60	3.08 ± 0.40	8.48 ± 0.65
NGC 1068 pos4	0.57 ± 0.35	-5.92 ± 0.80	1.22 ± 0.48	5.03 ± 0.77
NGC 1068 pos8a	2.46 ± 0.30	-4.73 ± 0.85	3.06 ± 0.54	6.48 ± 0.94
SBS 0335-052	1.05 ± 0.12	0.72 ± 0.17	0.44 ± 0.17	2.41 ± 0.27	-140 ± 51
NGC 1569	-0.11 ± 1.26	-1.50 ± 1.55	0.41 ± 0.85	4.04 ± 0.82	0.84 ± 0.33	5.58 ± 0.51	5.61 ± 1.19	0.80 ± 1.18	0.95 ± 0.40	-0.18 ± 0.69	3.45 ± 0.29	2.33 ± 0.21	...
NGC 1705	1.13 ± 0.08	1.72 ± 0.14	1.51 ± 0.13	3.27 ± 0.17	0.93 ± 0.12	5.10 ± 0.19	1.28 ± 0.25	0.76 ± 0.27	-85 ± 16
NGC 1741	1.84 ± 0.15	2.75 ± 0.21	2.18 ± 0.15	5.82 ± 0.17	1.16 ± 0.15	8.47 ± 0.21	1.27 ± 0.29	0.85 ± 0.38	-67 ± 21
NGC 2366 (NGC 2363)	-1.36 ± 0.74	0.27 ± 0.35
NGC 2366 (NGC 2363-a)	2.10 ± 0.18	0.58 ± 0.36	0.89 ± 0.30	-0.21 ± 0.37	0.35 ± 0.22	-3.16 ± 0.48	189 ± 68
NGC 2366 (NGC 2363-b)	0.60 ± 0.12	0.88 ± 0.24	0.80 ± 0.23	0.69 ± 0.30	0.31 ± 0.12	1.50 ± 0.20	-154 ± 29
NGC 2403 vs9	0.95 ± 0.63	1.32 ± 0.38	-0.54 ± 0.32	1.34 ± 0.22	1.99 ± 0.19	...
NGC 2403 vs38	1.53 ± 0.54	1.64 ± 0.41	-0.30 ± 0.34	3.12 ± 0.21	4.03 ± 0.18	...
NGC 2403 vs44	0.71 ± 0.39	1.60 ± 0.41	0.52 ± 0.26	2.72 ± 0.20	3.55 ± 0.15	...
He 2-10 A	2.93 ± 0.17	6.19 ± 0.19	2.44 ± 0.15	9.73 ± 0.25	-297 ± 30
He 2-10 B	2.72 ± 0.23	5.71 ± 0.28	2.21 ± 0.26	9.35 ± 0.39	-157 ± 24
IRAS 08339+6517	2.15 ± 0.15	3.56 ± 0.22	2.83 ± 0.17	4.87 ± 0.19	1.21 ± 0.13	6.90 ± 0.21	0.63 ± 0.24	0.06 ± 0.32	-241 ± 27
SBS 1415+437	-0.10 ± 0.90	0.02 ± 0.45
I Zw 18	1.23 ± 0.74	1.81 ± 0.59
I Zw 18 NW HII R	0.19 ± 0.78	1.07 ± 0.28
I Zw 18 SE HII R	-1.64 ± 1.05	-2.30 ± 0.53
NGC 3690	3.57 ± 0.25	-4.07 ± 0.94	3.85 ± 0.33	7.01 ± 0.41	2.23 ± 0.22	9.56 ± 0.30	2.36 ± 0.24	2.50 ± 0.22	4.38 ± 0.32	-6 ± 26
UM 469	6.58 ± 0.38	1.42 ± 0.27	0.12 ± 0.31	1.05 ± 0.32	5.09 ± 0.29	5.32 ± 0.26	6.49 ± 0.16	...
NGC 4038 405	3.02 ± 0.18	7.55 ± 0.27	1.46 ± 0.26	10.00 ± 0.34	29 ± 72
NGC 4038 442	3.31 ± 0.29	9.30 ± 0.41	2.96 ± 0.35	12.48 ± 0.47	-100 ± 75
NGC 4214	1.02 ± 0.18	1.36 ± 0.26	0.67 ± 0.25	2.69 ± 0.36	0.92 ± 0.15	6.39 ± 0.22	1.62 ± 0.17	0.37 ± 0.18	1.64 ± 0.28	33 ± 20
Tololo 1214-277	-2.88 ± 5.58	4.77 ± 2.91
NGC 4569	1.88 ± 0.40	5.15 ± 0.38	3.31 ± 0.23	7.91 ± 0.29	1.55 ± 0.22	8.06 ± 0.31	4.73 ± 0.46	1.53 ± 0.56	4.94 ± 0.39	7.63 ± 0.22	6.17 ± 0.15	7.69 ± 0.10	-141 ± 55
IC 3639	2.12 ± 0.20	0.77 ± 0.49	0.66 ± 0.37	6.41 ± 0.33	2.00 ± 0.29	-6.96 ± 1.18	-214 ± 37
NGC 4670	1.26 ± 0.15	2.78 ± 0.22	1.87 ± 0.18	4.52 ± 0.19	1.37 ± 0.15	7.63 ± 0.21	2.19 ± 0.16	0.62 ± 0.22	2.70 ± 0.27	32 ± 39
NGC 4861	1.22 ± 0.69	1.66 ± 0.30	-0.32 ± 0.37	0.12 ± 0.37	-0.66 ± 0.29	...
NGC 5055	1.41 ± 1.13	5.70 ± 1.20	1.41 ± 1.17	5.59 ± 1.18	-1.63 ± 1.75	1.58 ± 2.65	20.82 ± 6.71	-2.02 ± 1.85	3.34 ± 0.58	7.64 ± 0.41	6.14 ± 0.27	7.55 ± 0.17	...
NGC 5135	2.19 ± 0.21	4.39 ± 0.28	2.27 ± 0.27	8.76 ± 0.29	1.75 ± 0.23	8.81 ± 0.32	-137 ± 40
NGC 5253 HII R-1	0.11 ± 0.88	-0.10 ± 0.76
NGC 5253 HII R-2	2.89 ± 1.17	-1.65 ± 0.71
NGC 5253 UV1	1.72 ± 0.35	2.83 ± 0.56	2.72 ± 0.46	2.11 ± 0.59	1.65 ± 0.97	6.59 ± 1.58	1.98 ± 2.00	-0.72 ± 0.87	1.84 ± 0.52	3.02 ± 0.58	3.76 ± 0.39	5.28 ± 0.30	-15 ± 65
NGC 5253 UV2	1.76 ± 0.48	2.20 ± 0.74	1.22 ± 0.55	4.56 ± 0.58	2.48 ± 0.65	7.63 ± 1.07	-2.39 ± 1.88	1.09 ± 0.76	0.61 ± 0.59	5.40 ± 0.82	4.56 ± 0.51	5.27 ± 0.35	117 ± 93
NGC 5253 UV3	3.30 ± 0.43	4.30 ± 0.79	2.61 ± 0.64	6.86 ± 0.82	-0.49 ± 1.15	-2.89 ± 2.31	11.12 ± 3.63	-0.56 ± 1.61	0.17 ± 0.51	6.16 ± 0.75	5.29 ± 0.46	5.70 ± 0.35	...
Tololo 1345-420	0.40 ± 1.71	2.23 ± 1.57	5.11 ± 0.53	3.11 ± 0.56	3.83 ± 0.38	...
NGC 5457 (NGC 5455)	0.82 ± 0.30	1.14 ± 0.52	0.98 ± 0.26	3.26 ± 0.21	4.21 ± 0.15	...
NGC 5457 Searle 5	-0.90 ± 0.67	-11.59 ± 1.53	2.77 ± 0.44	5.45 ± 0.62	1.15 ± 0.38	11.65 ± 0.43	2.76 ± 0.42	0.10 ± 0.82	3.07 ± 0.89	2.90 ± 0.72	3.34 ± 0.52	4.79 ± 0.46	...
NGC 5457 (NGC 5471)	1.79 ± 1.43	2.01 ± 0.82	0.93 ± 0.89	1.80 ± 0.55	-0.00 ± 0.72	...
NGC 7130	2.20 ± 0.21	4.31 ± 0.28	2.84 ± 0.23	9.11 ± 0.26	1.77 ± 0.28	6.66 ± 0.52	-499 ± 55
NGC 7552	3.64 ± 0.23	3.71 ± 0.30	5.02 ± 0.21	9.77 ± 0.27	3.06 ± 0.16	11.80 ± 0.24	1.82 ± 0.23	2.33 ± 0.32	5.87 ± 0.32	-174 ± 30
NGC 7714	2.02 ± 0.10	3.11 ± 0.16	2.63 ± 0.17	6.31 ± 0.18	1.78 ± 0.14	9.82 ± 0.20	1.74 ± 0.21	-6 ± 16

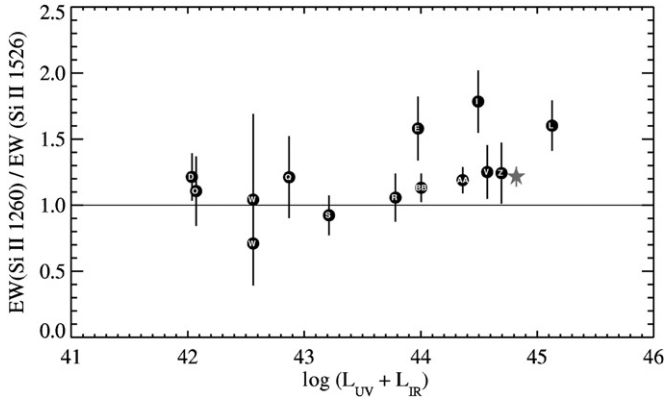


Figure 14. Ratio of the EWs of the Si II $\lambda 1260$ and $\lambda 1526$ lines vs. the intrinsic UV luminosity. The line ratio is ~ 2.5 and ~ 1.0 in the optically thin and the optically thick case, respectively. The asterisk denotes the location of the Lyman-break galaxy MS 1512-cB58. Individual galaxies are labeled by their identifiers defined in Table 2.

The EW of a given interstellar line depends on several factors: the column of gas along the line of sight, the covering factor of the gas, the abundance of the element, the fraction of the atoms in the appropriate ionization state, the transition probability (oscillator strength), and the velocity distribution of the gas. However, when the lines become strongly saturated, the EW depends mainly on the velocity distribution and the covering

factor of the gas. Unfortunately, the instrumental resolution of our spectra (a few 100 km s^{-1}) is insufficient to determine if the lines are saturated directly from their line profiles. However, because the strong Si II $\lambda 1260$ and $\lambda 1526$ lines have oscillator strengths that differ by a factor of ~ 8 , the ratio of their EWs provides a quick test. On the linear part of the curve of growth $\text{EW}(\text{Si II } \lambda 1260)/\text{EW}(\text{Si II } \lambda 1526) \approx 5.2$, whereas our spectra have ratios ranging from ~ 0.5 to 2, as shown in Figure 14. This suggests that Si II transitions are generally close to being optically thick. The same is likely to be true for the other strong low-ionization lines.

In Figure 15, we plot the line EWs of our nine new interstellar line indices versus metallicity. We also included in this figure the EWs measured for the three lensed Lyman-break galaxies MS 1512-cB58, the Cosmic Horseshoe, and the Eight O’clock Arc. Only data points with errors of less than 1.5 \AA are shown. For comparison, we indicate the median EWs of the Milky Way ISM lines as reported by Savage et al. (2000). Given the complex factors governing the line EWs, correlations with metallicity are not a priori expected. However, strong trends are evident in the Si II_1260, O I_Si II_1303, and C II_1335 indices, in agreement with the findings of H98 for the sum of these features. An additional line whose EW appears to be well correlated with metallicity is Si II $\lambda 1526$. The Al II_1670 index is generally too noisy to be very useful. While this line is nearly as strong as the Si and C features, the continuum estimation in this heavily line-blanked region of the spectrum is rarely satisfactory. The

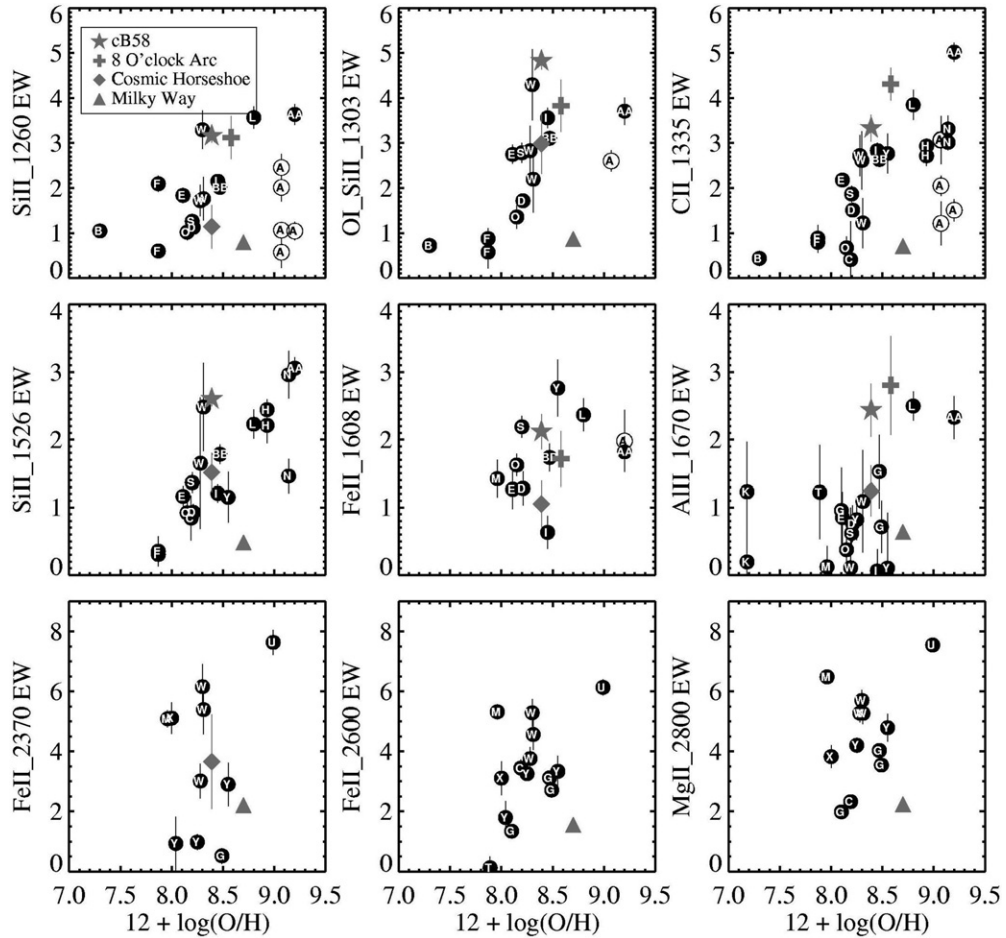


Figure 15. Equivalent widths of the interstellar lines vs. metallicity. The gray triangle indicates the median EW of the Milky Way ISM absorption as reported by Savage et al. (2000). The asterisk denotes MS 1512-cB58. The cross and the square indicate the Eight O’clock Arc and the Cosmic Horseshoe, respectively. Active galactic nuclei are highlighted with open symbols. Individual galaxies are labeled by their identifiers defined in Table 2.

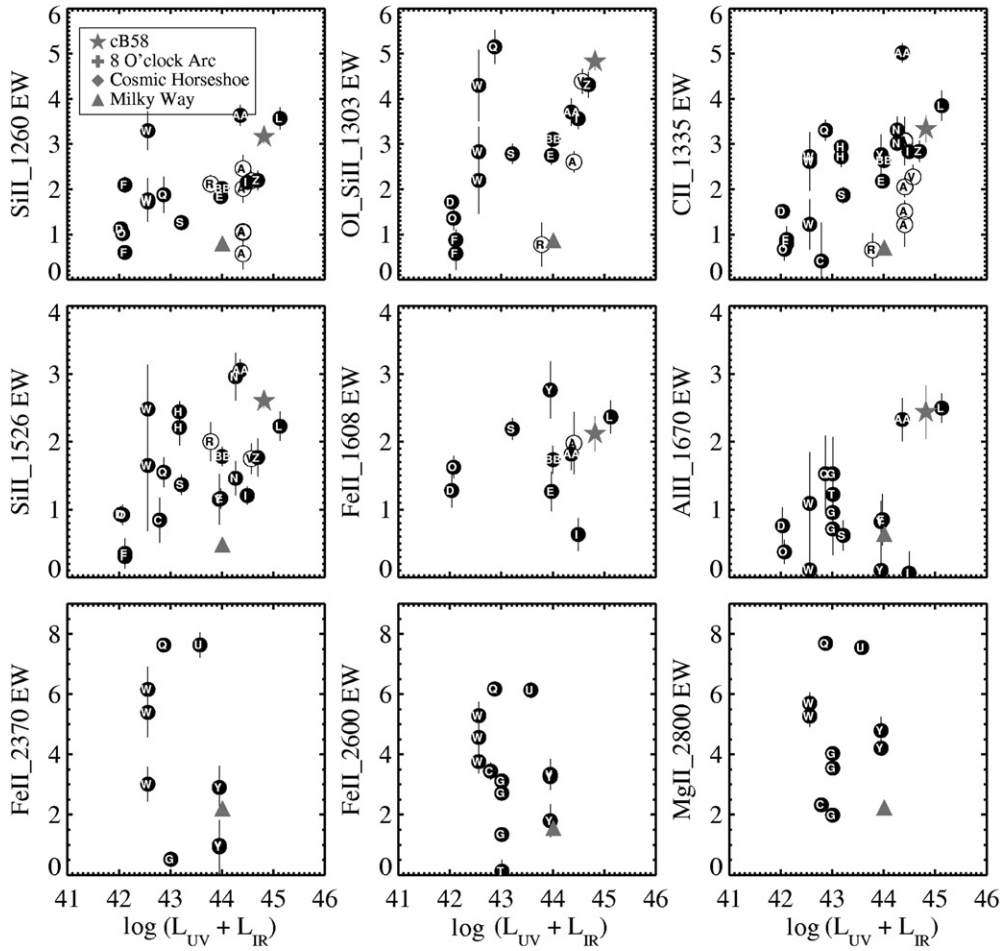


Figure 16. Equivalent widths of the interstellar lines vs. the intrinsic UV luminosity of the starburst, as parameterized by the sum of the far-UV and far-IR luminosities. Symbols and notations are the same as in Figure 15.

weaker Fe II $\lambda 1608$ line also suffers from these problems to some degree. Unfortunately, the spread in metallicity of the galaxies for which near-UV spectra were obtained is not large, so no reliable conclusions can be drawn about the usefulness of the FeII_2370, FeII_2600, and MgII_2800 indices.

In Figure 15, we included data points from the $z = 2.73$ lensed Lyman-break galaxy MS 1512-cB58. We measured the line indices of MS 1512-cB58 from a spectrum kindly provided by Max Pettini (Pettini et al. 2000). Also included in this figure are the results for the Lyman-break template of Shapley et al. (2003) where we measured the indices in the same way and assume its average metal abundance to be identical to that of MS 1512-cB58. Good agreement is seen between the high-redshift galaxies and our low-redshift sample, with a slight tendency for MS 1512-cB58 to have stronger UV lines than local galaxies of the same metallicity.

The origin of the correlation between the ISM line EW and metallicity is somewhat perplexing given the very different star-forming environments spanned by our sample. If the ISM lines were unsaturated (i.e., on the linear part of the curve of growth), the trend with metallicity would imply similar gas columns in the starbursts. This seems fairly implausible given that our sample includes SA galaxies like NGC 5055 as well as unevolved gas-rich dwarfs such as I Zw 18. A more plausible explanation is that the ISM lines tend to be saturated (as suggested by the Si II $\lambda 1260/\lambda 1526$ ratio) and that the correlation with metallicity is a secondary effect. As discussed previously, more metal-rich

galaxies tend to host more powerful starbursts which are likely to deposit more energy into the ISM, thereby increasing the turbulent velocity dispersion.

In Figure 16, we show the relation between ISM line EW and the intrinsic UV luminosity of the starburst, $L_{\text{UV}} + L_{\text{IR}}$. The SII_1260, OI_SII_1303, CII_1335, and SII_1526 indices all display good correlations. The FeII_1608 index shows a hint of an anti-correlation. We note, once again, the excellent agreement of the Lyman-break galaxies with the trends defined by the local galaxies. While an examination of trends in the ISM line EWs is illuminating, it does not take advantage of the superior resolution of the *HST* data. At *HST*'s resolution, kinematical studies of the gas become possible: bulk inflows or outflows of the gas can be measured relative to the photospheric features, and the turbulent velocity of the ISM can be inferred from the line widths. While the ISM line profiles are not fully resolved in the *HST* data, many of our sample spectra exhibit line widths well in excess of the instrumental resolution. Also, because we sample transitions with different oscillator strengths, some information about the Doppler broadening can in principle be recovered. We have therefore attempted to model the ISM absorption in each spectrum using a very simple prescription.

7.3. Line Profiles and Velocity Measurements

We fitted the line profiles of the ISM lines between 1200 and 1700 Å using a model with three free parameters: the total column density of H I, the turbulent velocity (Doppler

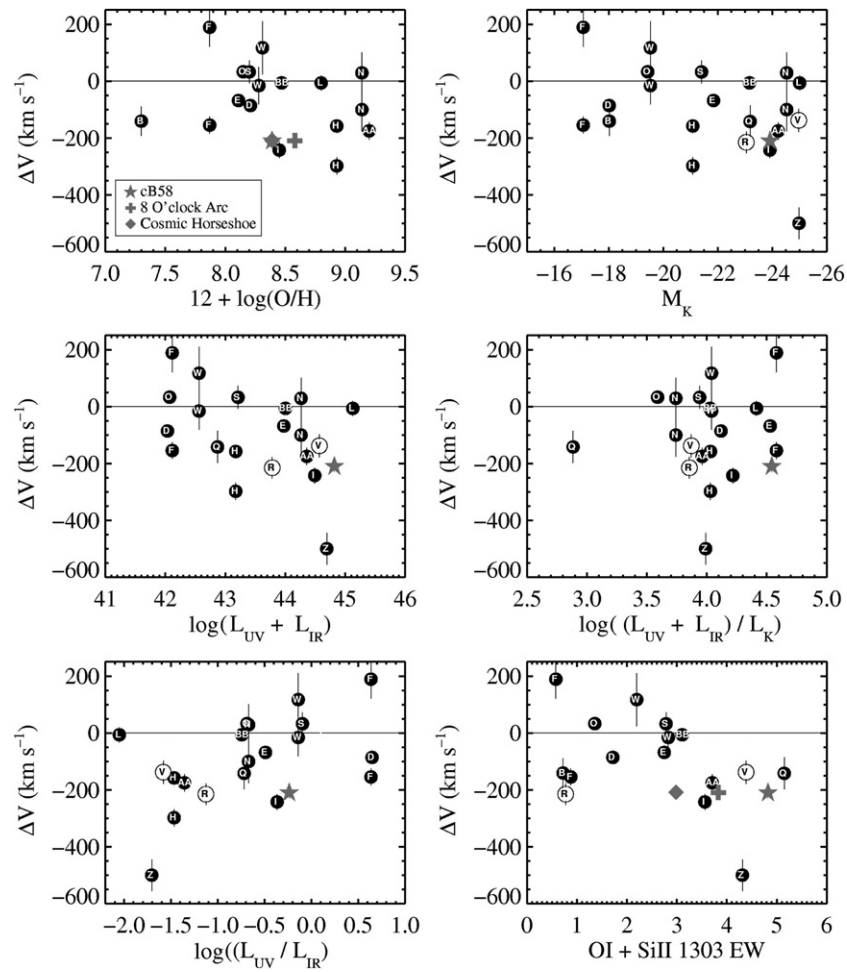


Figure 17. Correlation of the velocity offset with various galaxy parameters. Top left: oxygen abundance; top right: M_K ; middle left: intrinsic UV luminosity; middle right: burst strength as expressed by the ratio of young over old stars; bottom left: absorption of UV light by dust; bottom right: EW of the interstellar lines. Symbols and notations are the same as in Figure 15.

b parameter), and the velocity offset of the lines. This made the implicit assumption that gas at different ionization stages has the same velocity profile. However, we mitigated this by only performing the actual fit of the model over spectral regions encompassing the first ions—Si II $\lambda 1260$, Si II $\lambda 1304$, C II $\lambda 1335$, Si II $\lambda 1526$, Fe II $\lambda 1608$, Al II $\lambda 1670$. The other simplifying assumption we make is that the relative abundances of the elements in the gas phase are the same as the solar values reported by Meléndez & Asplund (2008). The oxygen abundance of the gas was then scaled to match the measured nebular metallicity. The implicit assumptions built into this approach are that the α -enhancement is similar to the solar pattern (although it only affects Fe II $\lambda 1608$) that the refractory nature of the elements does not change strongly with metallicity, and that ionization corrections are not required. While these assumptions are unlikely to hold in detail, they are reasonable approximations given the quality of the data. The final step in constructing the models was to convolve the synthetic spectra to the appropriate instrumental resolution. However, as discussed in Section 3, the instrumental resolution is not well known for our spectra. We assumed a resolution of 250 km s⁻¹ for the FOS spectra and 160 km s⁻¹ for the GHRS spectra, except for the NGC 1705 data where we use 120 km s⁻¹. This assumption is likely to be a source of error in the derived b parameter.

We now turn to examining how the measured velocity dispersions and velocity offsets correlate with galaxy physical

properties. In this analysis, we include only data where the model fit converged and where a by-eye inspection suggested that the fit was reasonable. We note that at our velocity resolution there is a certain amount of degeneracy expected between the derived gas column and the Doppler b parameter. However, the velocity offsets are completely robust to this degeneracy.

In Figure 17, we show how the velocity offsets relate to various host galaxy parameters. The velocity offsets are measured relative to the weak photospheric features as described in Section 3. There appears to be no strong trend in the velocity offset with rotation speed or starburst luminosity. However, it is interesting to note that galaxies with large absolute values of the velocity offsets (>100 km s⁻¹) have starburst luminosities greater than 10^{43} erg s⁻¹ (corresponding to star formation rates larger than $0.2 M_\odot$ yr⁻¹). This could be interpreted as evidence of a threshold star formation rate needed to drive a galactic wind. A correlation between outflow velocity as measured with the optical Na I D lines and the global star formation rate in starburst galaxies was suggested by Martin (2005) and Rupke et al. (2005). Chen et al. (2010) found a similar but weaker trend in a sample of star-forming galaxies drawn from Sloan Digital Sky Survey Data Release 7. This is consistent with theoretical expectations for the velocity of a swept-up shell of gas at the point where it blows out of the disk. However, more data are clearly necessary for a definitive conclusion.

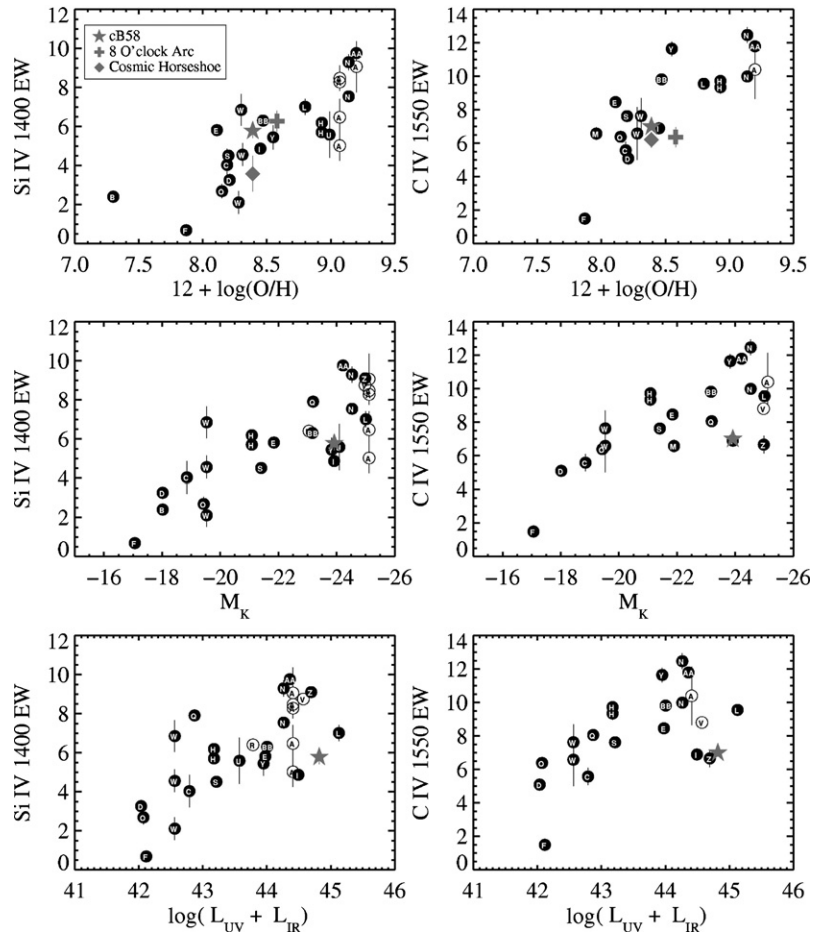


Figure 18. Correlation of the stellar-wind lines Si IV (left) and C IV (right) with various galaxy parameters. Top: oxygen abundance; middle: M_K ; bottom: intrinsic UV luminosity. Symbols and notations are the same as in Figure 15.

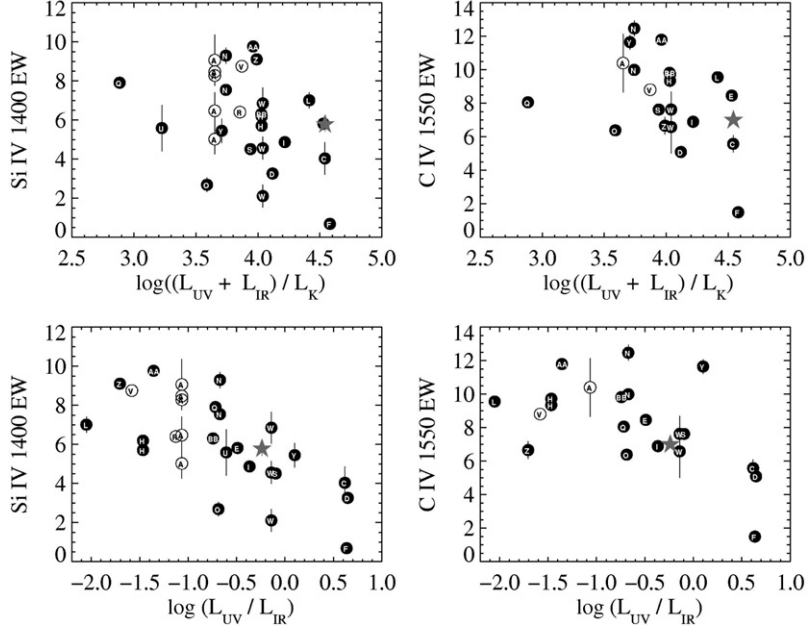


Figure 19. Similar to Figure 18, but for the correlation with burst strength (upper panels) and absorption of UV light by dust (lower panels.)

7.4. Stellar-wind Lines

Next, we examine how the properties of the stellar-wind lines depend upon the starburst luminosity and metallicity. We

utilize the SiIV_1400 and CIV_1550 line indices defined in Table 7 to characterize the *absorption* component of the SiIV and CIV stellar-wind lines (see Figure 11 for an illustration). We have not used the Nv $\lambda 1240$ line, due to the difficulty

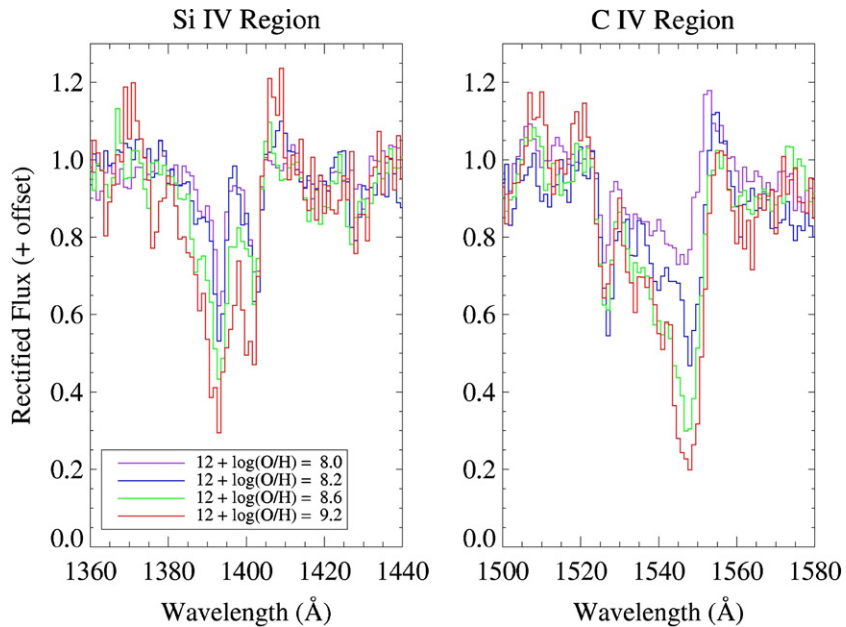


Figure 20. Illustration of the effect of metallicity on the stellar-wind lines Si iv $\lambda 1400$ (left) and C iv $\lambda 1550$ (right). The four sets of spectra shown are averages of four to seven individual galaxies. The mean oxygen abundances of the four sets are listed in the left panel.
(A color version of this figure is available in the online journal.)

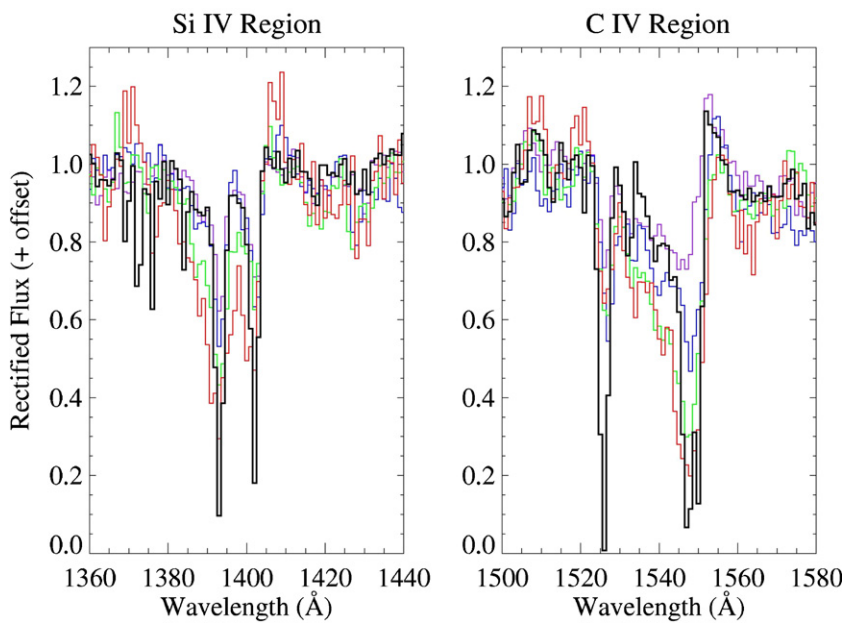


Figure 21. Comparison of the Si iv (left) and C iv (right) line profiles of MS 1512-cB58 (black) with the template spectra shown in Figure 20. The color coding of the templates is the same as in Figure 20. The metallicity of MS 1512-cB58, as derived from the strong-line method, is $12 + \log(\text{O/H}) = 8.4$ (Teplitz et al. 2000).
(A color version of this figure is available in the online journal.)

of measuring the continuum in such close proximity to the Ly α absorption line. We note that the measured Si iv and C iv features are not always stellar in origin but include large—sometimes dominant—contributions from interstellar absorption at Si iv $\lambda\lambda 1394, 1402$ and C iv $\lambda\lambda 1548, 1551$. In Figure 18 and 19, we show the correlation of the EWs of the Si iv and C iv features with several galaxy properties. As demonstrated by H98, there is a clear increase in the EW of the stellar-wind lines with starburst luminosity and metallicity.

It is clear that the properties of hot-star winds must depend upon metallicity because the winds are driven via photon

momentum transfer through metal-line absorption. The strength of the N v $\lambda 1240$, Si iv $\lambda 1400$, and C iv $\lambda 1550$ P-Cygni features in individual O and B stars is set by the mass-loss rate, which theoretical and observational results suggest scales as $\dot{M} \propto Z^{0.5-1.0}$ (Vink et al. 2001; Mokiem et al. 2007). However, the situation in composite stellar populations is complicated by the fact that the stellar-wind line profiles also depend strongly on the effective temperature and luminosity class of the ionizing star. The wind features in galaxy spectra therefore reflect the make-up of the stellar population (age, IMF) as well as the metallicity (Leitherer et al. 2001). Unfortunately, there is a certain amount of degeneracy between these effects since both

metal-poor and old stellar populations will show weak stellar-wind features.

The age–metallicity degeneracy problem is of particular relevance to our present study because the *HST* spectra are primarily dominated by the light of individual star clusters which are likely to contain stellar populations with discrete ages. Given this fact, the existence of a trend in the Si IV and C IV line strength with metallicity is remarkable. There are several reasons why this might occur. First, the *HST* targets selected where generally those with the highest UV brightness. This would tend to preferentially select very young clusters since their 1500 Å luminosities peak at about 3 Myr and decline rapidly thereafter. Young ages are clearly suggested for most of the spectra shown in Section 3 by the existence of strong C IV P-Cygni emission. The second possibility is that the interstellar components of Si IV and C IV are driving the observed trend since a correlation between interstellar line EW and metallicity was demonstrated in Figure 15.

Once again, the line profile information available with *HST*'s superior resolution provides insight. Figure 20 shows the Si IV and C IV line profiles of template spectra constructed by averaging spectra of similar metallicities. The range in metallicity is from 1/5 solar to nearly three times solar. While it is difficult to gauge the exact interstellar contribution to the Si IV and C IV lines, the asymmetric blueshifted portion of the lines can clearly be attributed to stellar winds. Notably, the stellar and interstellar contributions appear to scale roughly in lock step. Even at the lowest metallicities, very broad blueshifted components are evident. Visual inspection of the profiles suggests that the interstellar component could plausibly account for ∼2/3 of the Si IV EW and ∼1/3 of the C IV EW. Clearly, both the stellar and interstellar components contribute to the observed scaling of the line EWs with metallicity.

Besides mitigating the effects of the stellar population age on the observed Si IV and C IV features, another positive side effect of the blend of stellar and interstellar features is that the line strengths of the combined features are nearly double that of the pure interstellar features. Thus, the Si IV and C IV lines can serve as valuable metallicity diagnostics even in spectra with relatively poor S/N. This fact has already been taken advantage of for mapping the chemical enrichment history of the universe. Mehrt et al. (2002) used the C IV EW measured from 57 Very Large Telescope spectra of galaxies at redshifts from 1.37 to 3.4 to infer the evolution of the mean cosmic metallicity at these epochs. However, some caution is in order due to the composite nature of the lines. In Figure 21, we compare the spectrum of the lensed Lyman-break galaxy MS 1512-cB58 with the metallicity templates shown in Figure 20. The stellar-wind features match moderately well with the two low-metallicity templates ($12 + \log(\text{O/H}) = 8.0$ and 8.2), but the interstellar features appear much stronger. The results in this figure suggest care when interpreting absorption features containing both interstellar and stellar contributions. Crowther et al. (2006) found that for the C IV profile to give reliable abundances at high redshift, its usage should be limited to data of sufficiently high spectral resolution ($>300 \text{ km s}^{-1}$) in order to separate the stellar and interstellar C IV components. Oxygen abundances will be systematically overestimated if the local calibration is applied to spectra of high-redshift galaxies obtained at lower resolution, as is typical for many current wide-field surveys.

Ironically, the well-studied, archetypal Lyman-break galaxy MS 1512-cB58 may have rather atypical interstellar line strengths for its general properties. Heckman et al. (2001) mea-

sured residual intensities in the line cores of the UV interstellar lines of a few percent. The corresponding EWs are about a factor of two higher than the average of the Lyman-break sample discussed by Steidel et al. (2001). The reason for the difference is not understood and may hint at the diversity of the ISM in high-redshift galaxies.

8. CONCLUSIONS

We have presented 46 UV spectra of local starburst and star-forming galaxies obtained with *HST*'s legacy instruments FOS and GHRS through ∼1–2 arcsec apertures with a spectral resolution of a few 100 km s⁻¹. These observations provide a unique data set to study local starbursts due to the specific spatial scales that they probe. Earlier observations through the large *IUE* aperture sample starburst sizes of order ∼1 kpc. In contrast, STIS, one of *HST*'s current UV spectrographs probes scales as small as a few pc. FOS and GHRS bridge this gap by observing multi-cluster regions extending over tens of pc. When compared at the same resolution, *HST* and *IUE* spectra show some substantial differences. However, these differences are not random, but systematic, and fully consistent with our expectation based on the aperture differences. The star clusters sampled by the *HST* spectra provide about 15% of the UV luminosity measured by *IUE*. Their spectra are bluer and have stronger stellar-wind features than the starburst as a whole. This suggests either that the clusters observed by *HST* are the youngest pieces of the burst, or that a significant amount of light from an older stellar generation contributes to the *IUE* spectrum. Interestingly, the interstellar lines appear to be generally consistent in the *IUE* and *HST* spectra, which is evidence of similar ISM properties along most sightlines. Under the assumption that the ISM lines are saturated, the lack of any systematic differences implies a turbulent rather than rotational origin for the line widths. Altogether, the nature and degree of differences between the small-aperture FOS and GHRS spectra and the large-aperture *IUE* spectra indicate that the *HST* spectra are suitable for our stated purpose of learning how UV spectral morphology correlates with galaxy physical properties.

The spectra presented in this work can be an invaluable tool for the interpretation of star-forming galaxies at any redshift, and they can test and complement theoretical spectral models. Efforts to interpret the UV spectra of galaxies tend to fall into three categories: comparison with observed galaxy templates, generation of synthetic spectra with observed stellar templates, and a fully theoretical approach using stellar model atmospheres. Each approach has its distinct pros and cons, and taken together they can identify shortcomings and provide guidance for improvement. The galaxy templates presented here cover the hitherto relatively unexplored spectral region between 2000 and 3000 Å. While this region is devoid of strong stellar-wind features, it contains numerous interstellar lines and a plethora of photospheric blends which can be used to constrain chemical abundances and other properties. The full wavelength region of our templates from 1150 to 3000 Å provides insight into the behavior of the four principal spectral-line types found: stellar-wind P-Cygni lines, photospheric absorption blends, narrow interstellar absorption, and nebular emission lines.

Numerous authors have highlighted the similarity between local starbursts and Lyman-break galaxies (Meurer et al. 1997; H98; Chandar et al. 2004; Grimes et al. 2006, 2007; Schwartz et al. 2006; Pettini 2008). Our atlas is suitable for comparisons with the most recent generation of high-redshift observations, whose wavelength coverage, S/N, and spectral resolution

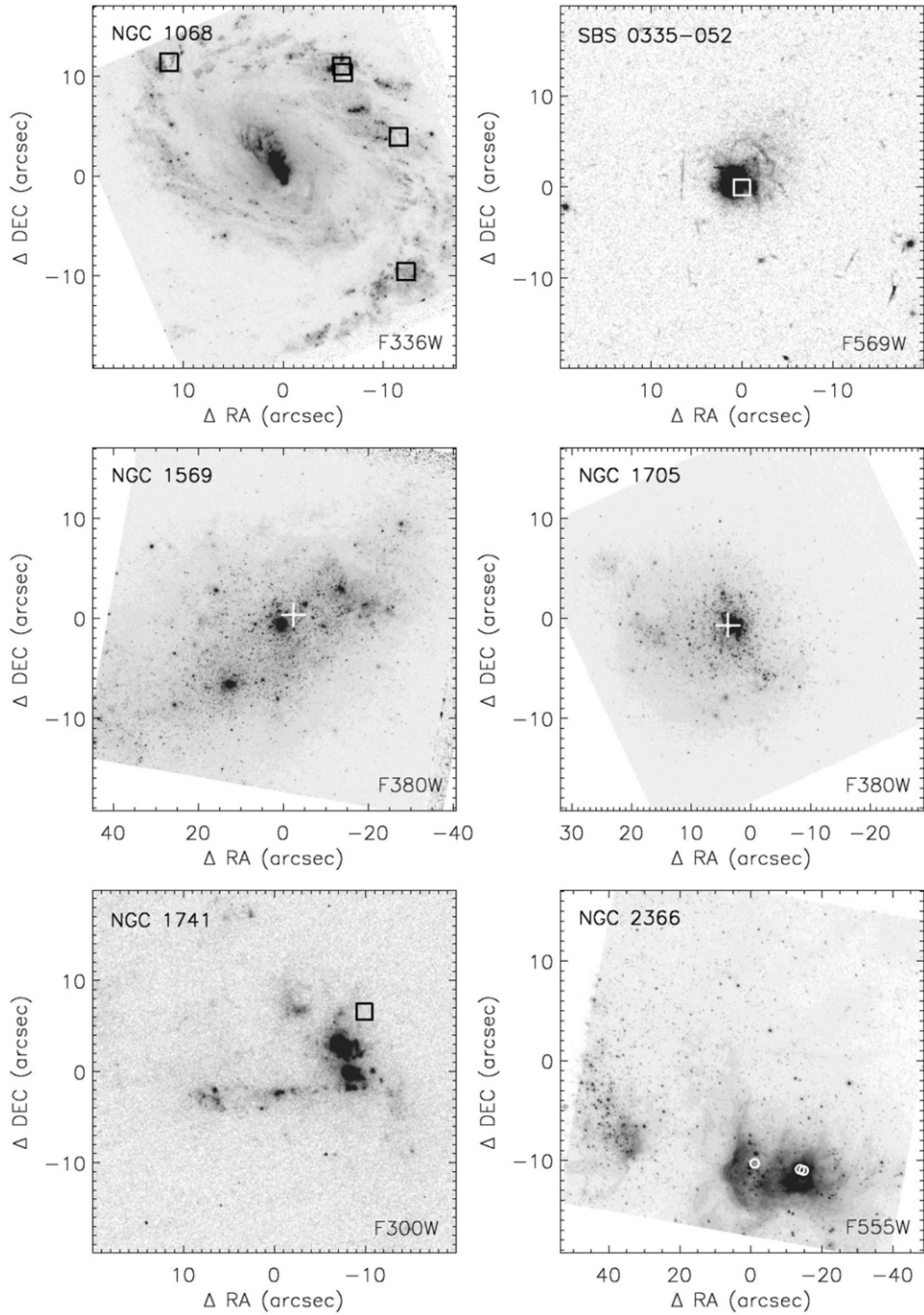


Figure A1. Images of the sample galaxies with the spectroscopic apertures overlaid. The aperture positions represent the initial target coordinates. A peak-up is used to center the aperture on the target. Apertures are shown to scale (black or white circles and squares). In some cases, cross-hairs have been added to make the apertures more visible. North is up and east to the left. Filters are listed in the lower right-hand corner.

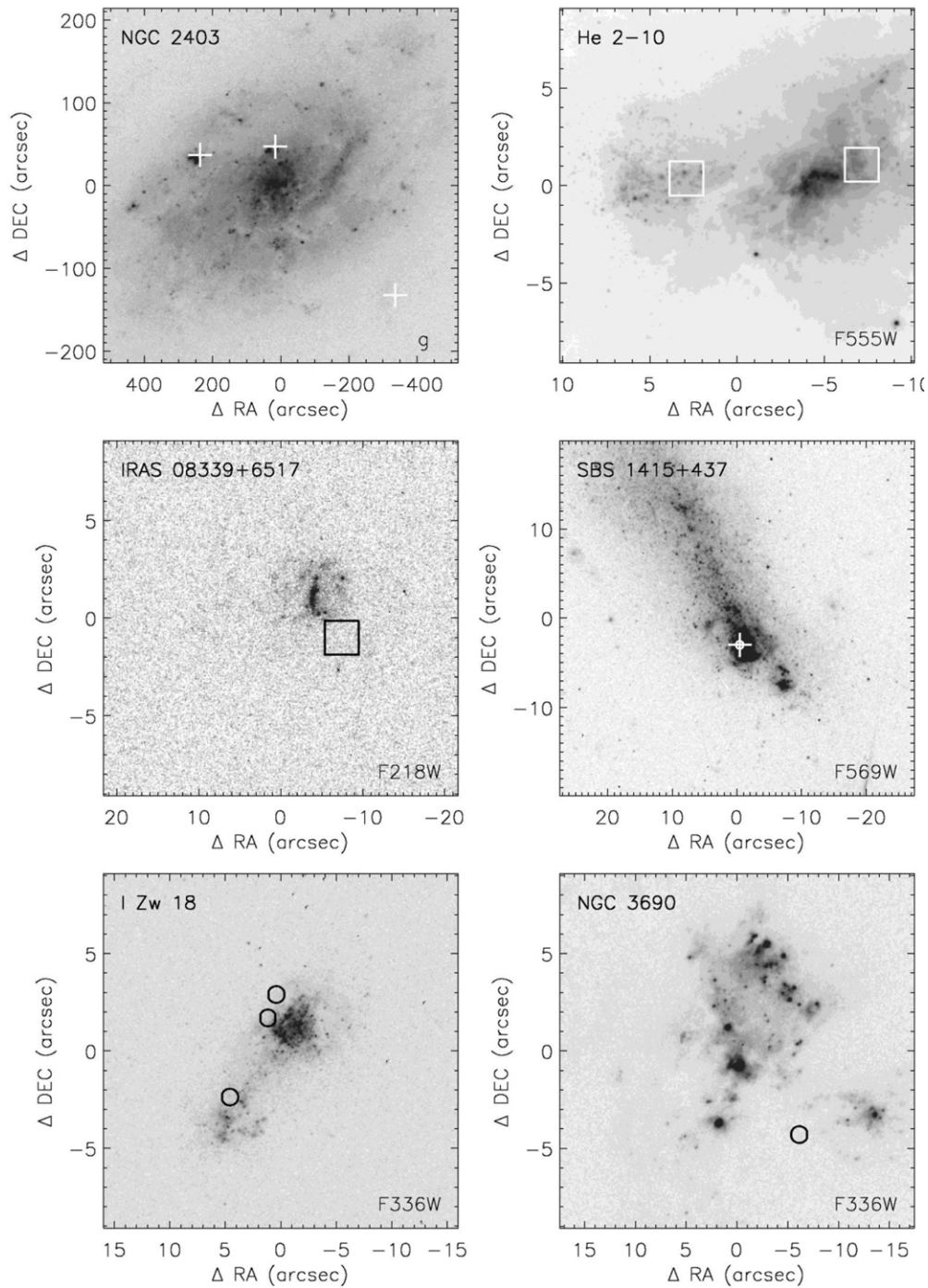
are close matches to the FOS and GHRS data. The spectra presented here are available in online form for download at <http://www.stsci.edu/science/starburst/templ.html>.

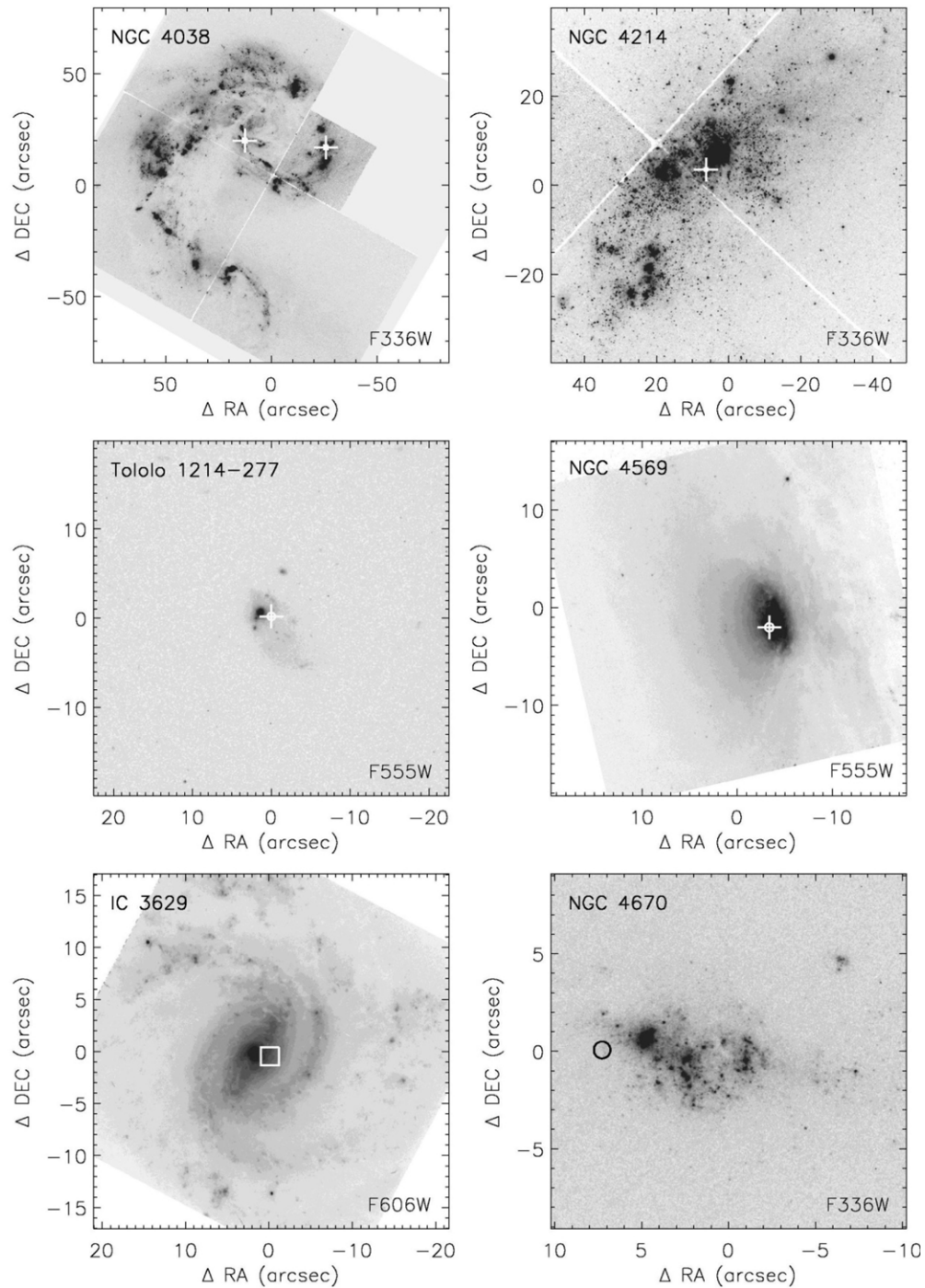
We thank Miroslava Dessauges-Zavadsky and Max Pettini for kindly providing electronic versions of the rest-frame UV spectra of the “Eight O’clock Arc” and the “Cosmic Horseshoe,” respectively. Support for this work has been provided by NASA through grant number AR-08348.01-97 from the Space Telescope Science Institute, which is operated by AURA, Inc., under NASA contract NAS5-26555. This work has made extensive use of the NASA/IPAC extragalactic database (NED), which is

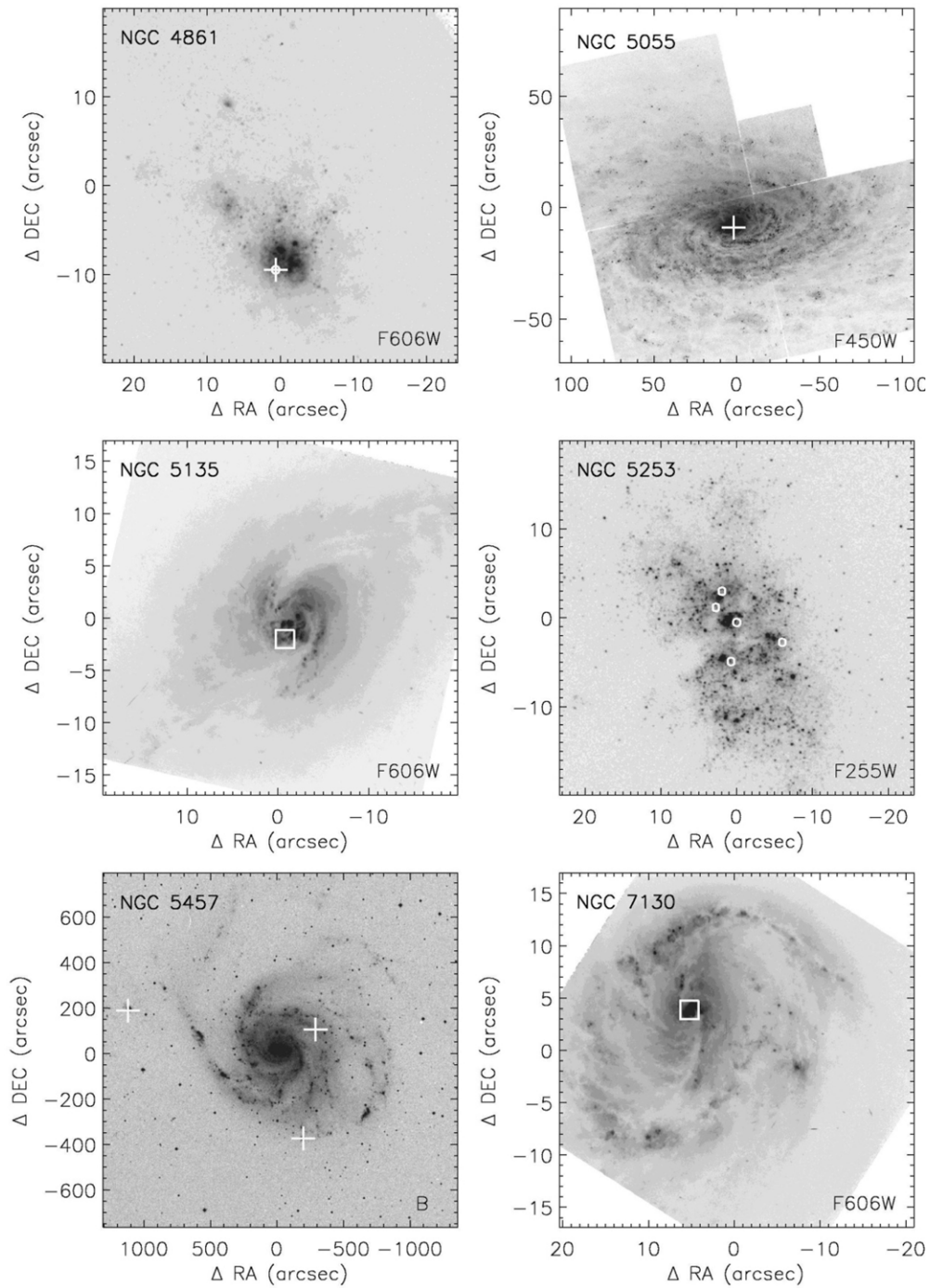
operated by the Jet Propulsion Laboratory, Caltech, under contract with the National Aeronautics and Space Administration. We also utilized the Atomic Line List (v2.04) maintained by Peter van Hoof at <http://www.pa.uky.edu/~peter/atomic/>. We thank Ed Jenkins for clarifying discussions on the importance of Galactic high-velocity clouds.

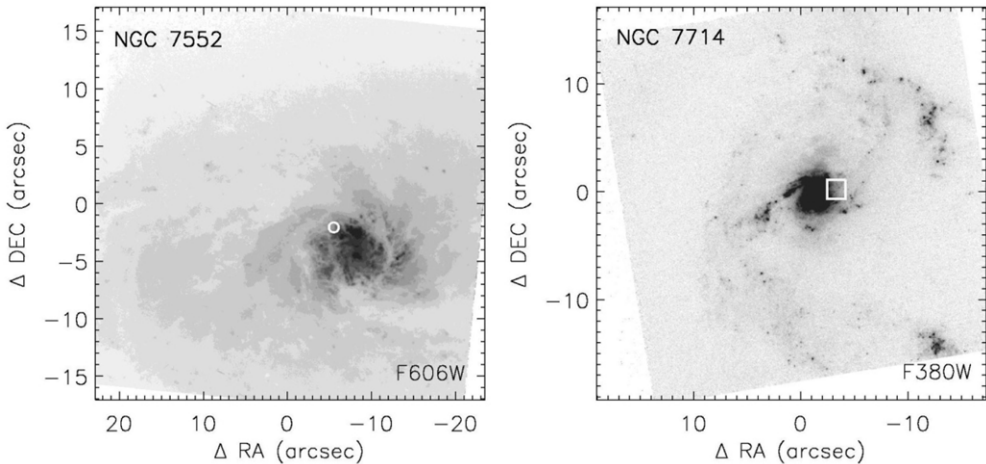
APPENDIX

For reference we show images of our sample galaxies with the spectroscopic apertures overlaid. The images were obtained from the *HST* archive and from the NASA/IPAC Extragalactic Database (NED). Where multi-color data were available, we

**Figure A1.** (Continued)

**Figure A1.** (Continued)

**Figure A1.** (Continued)

**Figure A1.** (Continued)

selected observations near 3000\AA to best display the UV-optical morphology of the galaxies. All images were obtained with *HST*'s WFPC2 camera, except for NGC 2403 and NGC 5457, for which ground-based images were substituted due to their large apparent diameter. No useful images were available for UM 469 and Tololo 1345–420, both of which are highly compact sources. The absolute astrometry of the images is uncertain by at least $\pm 1''$. The position of the spectroscopic apertures shown in Figure A1 represents the initial target coordinates specified in the *HST* proposal. The spectroscopic targets are centered in the science apertures using an onboard acquisition procedure (Sections 3.2 and 3.3), hence final placement of the aperture is difficult to ascertain.

REFERENCES

- Aloisi, A., Van Der Marel, R. P., Mack, J., Leitherer, C., Sirianni, M., & Tosi, M. 2005, *ApJ*, **631**, L45
- Aloisi, A., et al. 2007, *ApJ*, **667**, L151
- Angeretti, L., Tosi, M., Greggio, L., Sabbi, E., Aloisi, A., & Leitherer, C. 2005, *AJ*, **129**, 2203
- Bastian, N., Emsellem, E., Kissler-Patig, M., & Maraston, C. 2006, *A&A*, **445**, 471
- Beichman, C., Neugebauer, G., Habing, H. J., Clegg, P. E., & Chester, T. J. 1988, in NASA RP-1190, Infrared Astronomical Satellite (IRAS) Catalogs and Atlases, Vol. 1: Explanatory Supplement (Washington, DC: GPO)
- Brandt, J. C., et al. 1994, *PASP*, **106**, 890
- Brandt, J. C., et al. 1998, *AJ*, **116**, 941
- Brinchmann, J., Charlot, S., White, S. D. M., Tremonti, C., Kauffmann, G., Heckman, T., & Brinkmann, J. 2004, *MNRAS*, **351**, 1151
- Calzetti, D. 2001, *PASP*, **113**, 1449
- Calzetti, D. 2008, in Pathways Through an Eclectic Universe, ed. H. Knapen, T. J. Mahoney, & A. Vazdekis (San Francisco, CA: ASP), 121
- Calzetti, D., Kinney, A. L., & Storchi-Bergmann, T. 1994, *ApJ*, **429**, 582
- Chandar, R., Leitherer, C., & Tremonti, C. A. 2004, *ApJ*, **604**, 153
- Chandar, R., Leitherer, C., Tremonti, C. A., & Calzetti, D. 2003, *ApJ*, **586**, 939
- Chen, H.-W., Prochaska, J. X., & Bloom, J. S. 2007, *ApJ*, **668**, 384
- Chen, Y.-M., Tremonti, C. A., Heckman, T. M., Kauffmann, G., Weiner, B. J., Brinchmann, J., & Wang, J. 2010, *AJ*, **140**, 445
- Cowie, L. L., Songaila, A., & Barger, A. J. 1999, *AJ*, **118**, 603
- Crowther, P. A., Prinja, R. K., Pettini, M., & Steidel, C. C. 2006, *MNRAS*, **368**, 895
- Dean, C. A., & Bruhweiler, F. C. 1985, *ApJS*, **57**, 133
- de Mello, D. F., Leitherer, C., & Heckman, T. M. 2000, *ApJ*, **530**, 251
- Dessauges-Zavadsky, M., D'Odorico, S., Schaefer, D., Modigliani, A., Tapken, C., & Vernet, J. 2010, *A&A*, **510**, A26
- de Vaucouleurs, G., de Vaucouleurs, A., Corwin, H. G., Jr., Buta, R. J., Paturel, G., & Fouque, P. 1991, Third Reference Catalogue of Bright Galaxies (New York: Springer), v3.9
- Ellingson, E., Yee, H. K. C., Bechtold, J., & Elston, R. 1996, *ApJ*, **466**, L71
- Esteban, C., Peimbert, M., Torres-Peimbert, S., & Rodríguez, M. 2002, *ApJ*, **581**, 241
- Ferrarese, L., et al. 2000, *ApJS*, **128**, 431
- Finkelstein, S. L., Papovich, C., Rudnick, G., Egami, E., LeFloc'h, E., Rieke, M. J., Rigby, J. R., & Willmer, C. N. A. 2009, *ApJ*, **700**, 376
- Fitzpatrick, E. L. 1999, *PASP*, **111**, 63
- Garnett, D. R. 1999, in IAU Symp. 190, New Views of the Magellanic Clouds, ed. Y.-H. Chu, N. Suntzeff, J. Hesser, & D. Bohlender (San Francisco, CA: ASP), 266
- Garnett, D. R. 2002, *ApJ*, **581**, 1019
- Garnett, D. R., Shields, G. A., Peimbert, M., Torres-Peimbert, S., Skillman, E. D., Dufour, R. J., Terlevich, E., & Terlevich, R. J. 1999, *ApJ*, **513**, 168
- Garnett, D. R., Shields, G. A., Skillman, E. D., Sagan, S. P., & Dufour, R. J. 1997, *ApJ*, **489**, 63
- Gil de Paz, A., et al. 2007, *ApJS*, **173**, 185
- González-Delgado, R. M., Pérez, E., Díaz, A. I., García-Vargas, M. L., Terlevich, E., & Vílchez, J. M. 1995, *ApJ*, **439**, 604
- Grimes, J. P., Heckman, T., Hoopes, C., Strickland, D., Aloisi, A., Meurer, G., & Ptak, A. 2006, *ApJ*, **648**, 310
- Grimes, J. P., et al. 2007, *ApJ*, **668**, 891
- Grimes, J. P., et al. 2009, *ApJS*, **181**, 272
- Hainline, K. N., Shapley, A. E., Kornei, K. A., Pettini, M., Buckley-Geer, E., Allam, S. S., & Tucker, D. L. 2009, *ApJ*, **701**, 52
- Halliday, C., et al. 2008, *A&A*, **479**, 417
- Harms, R. J., et al. 1979, Proc. SPIE, **183**, 74
- Heckman, T. M., & Leitherer, C. 1997, *AJ*, **114**, 69
- Heckman, T. M., Robert, C., Leitherer, C., Garnett, D. R., & Van Der Rydt, F. 1998, *ApJ*, **503**, 646 (H98)
- Heckman, T. M., Sembach, K. R., Meurer, G. R., Leitherer, C., Calzetti, D., & Martin, C. L. 2001, *ApJ*, **558**, 56
- Helou, G., Khan, I. R., Malek, L., & Boehmer, L. 1988, *ApJS*, **68**, 151
- Hopkins, A. M. 2004, *ApJ*, **615**, 209
- Huchra, J. P., Geller, M. J., Gallagher, J., Hunter, D., Hartmann, L., Fabbiano, G., & Aaronson, M. 1983, *ApJ*, **274**, 125
- Huchtmeier, W. K., & Richter, O.-G. 1989, A General Catalog of H I Observations of Galaxies. The Reference Catalog, XIX (Berlin: Springer)
- IRAS Point Source Catalog 1985, Joint IRAS Science Working Group (Washington, DC: GPO)
- Izotov, Y. I., Thuan, T. X., & Stasińska, G. 2007, *ApJ*, **662**, 15
- Jarrett, T. H., Chester, T., Cutri, R., Schneider, S. E., & Huchra, J. P. 2003, *AJ*, **125**, 525
- Karachentsev, I. D., et al. 2003, *A&A*, **398**, 479
- Kennicutt, R. C., Bresolin, F., & Garnett, D. R. 2003, *ApJ*, **591**, 801
- Kewley, L. J., & Ellison, S. L. 2008, *ApJ*, **681**, 1183
- Kinney, A. L., Bohlin, R. C., Calzetti, D., Panagia, N., & Wyse, R. F. 1993, *ApJS*, **86**, 5
- Kobulnicky, H. A., & Gebhardt, K. 2000, *AJ*, **119**, 1608
- Kobulnicky, H. A., Kennicutt, R. C., & Pizagno, J. L. 1999, *ApJ*, **514**, 544
- Kobulnicky, H. A., & Skillman, E. D. 1997, *ApJ*, **489**, 636
- Kobulnicky, H. A., & Skillman, E. D. 1998, *ApJ*, **497**, 601
- Kudritzki, R.-P., & Puls, J. 2000, *ARA&A*, **38**, 613
- Kunth, D., Mas-Hesse, J. M., Terlevich, E., Terlevich, R., Lequeux, J., & Fall, S. M. 1998, *A&A*, **334**, 11

- Lauberts, A., & Valentijn, E. A. 1989, The Surface Photometry Catalogue of the ESO-Uppsala Galaxies (Garching: European Southern Observatory)
- Lee, H., & Skillman, E. D. 2004, *ApJ*, **614**, 698
- Leitherer, C. 2010, in UP2010: Have Observations Revealed a Variable Upper End of the Initial Mass Function, ed. M. Treyer, J. C. Lee, M. H. Seibert, T. Wyder, & D. Neill (San Francisco, CA: ASP), in press
- Leitherer, C., & Chen, J. 2009, *New Astron.*, **14**, 356
- Leitherer, C., Leão, J. R. S., Heckman, T. M., Lennon, D. J., Pettini, M., & Robert, C. 2001, *ApJ*, **550**, 724
- Leitherer, C., Li, I.-H., Calzetti, D., & Heckman, T. M. 2002, *ApJS*, **140**, 303
- Leitherer, C., Ortiz Otálvaro, P. A., Bresolin, F., Kudritzki, R.-P., Lo Faro, B., Pauldrach, A. W. W., Pettini, M., & Rix, S. A. 2010, *ApJS*, **189**, 309
- Leitherer, C., et al. 1999, *ApJS*, **123**, 3
- Lilly, S. J., Le Fevre, O., Hammer, F., & Crampton, D. 1996, *ApJ*, **460**, L1
- López-Sánchez, Á., Esteban, C., & García-Rojas, J. 2006, *A&A*, **449**, 997
- López-Sánchez, Á., Esteban, C., García-Rojas, J., Peimbert, M., & Rodríguez, M. 2007, *ApJ*, **656**, 168
- Maíz-Apellániz, J., Cieza, L., & MacKenty, J. W. 2002, *AJ*, **123**, 1307
- Martin, C. L. 2005, *ApJ*, **621**, 227
- Mehlert, D., et al. 2002, *A&A*, **393**, 809
- Meléndez, J., & Asplund, M. 2008, *A&A*, **490**, 817
- Meurer, G. R., Heckman, T. M., & Calzetti, D. 1999, *ApJ*, **521**, 64
- Meurer, G. R., Heckman, T. M., Lehnert, M. D., Leitherer, C., & Lowenthal, J. 1997, *AJ*, **114**, 54
- Meurer, G. R., Staveley-Smith, L., & Killeen, N. E. B. 1998, *MNRAS*, **300**, 705
- Mokiem, M. R., et al. 2007, *A&A*, **473**, 603
- Moshir, M., et al. 1993, VizieR Online Data Catalog
- Mould, J. R., et al. 2000, *ApJ*, **529**, 786
- Moustakas, J., Kennicutt, R. C., Tremonti, C. A., Dale, D. A., Smith, J. D. T., & Calzetti, D. 2010, *ApJS*, **190**, 233
- Nava, A., Casebeer, D., Henry, R. B. C., & Jevremovic, D. 2006, *ApJ*, **645**, 1076
- Papovich, C., Dickinson, M., & Ferguson, H. C. 2001, *ApJ*, **559**, 620
- Pérez-González, P. G., et al. 2008, *ApJ*, **675**, 234
- Pettini, M. 2008, in IAU Symp. 250, Massive Stars as Cosmic Engines, ed. F. Bresolin, P. A. Crowther, & J. Puls (Cambridge: Cambridge Univ. Press), 415
- Pettini, M., Rix, S. A., Steidel, C. C., Adelberger, K. L., Hunt, M. P., & Shapley, A. E. 2002, *ApJ*, **569**, 742
- Pettini, M., Steidel, C. C., Adelberger, K. L., Dickinson, M., & Giavalisco, M. 2000, *ApJ*, **528**, 96
- Prochaska, J. X., et al. 2001, *ApJS*, **137**, 21
- Puls, J., Vink, J. S., & Najarro, F. 2008, *A&AR*, **3–4**, 209
- Quider, A. M., Pettini, M., Shapley, A. E., & Steidel, C. C. 2009, *MNRAS*, **398**, 1263
- Rice, W., Lonsdale, C. J., Soifer, B. T., Neugebauer, G., Kopan, E. L., Lloyd, L. A., de Jong, T., & Habing, H. J. 1988, *ApJS*, **68**, 91
- Rix, S. A., Pettini, M., Leitherer, C., Bresolin, F., Kudritzki, R. P., & Steidel, C. C. 2004, *ApJ*, **615**, 98
- Robert, C., Pellerin, A., Aloisi, A., Leitherer, C., Hoopes, C., & Heckman, T. M. 2003, *ApJS*, **144**, 21
- Rupke, D. S., Veilleux, S., & Sanders, D. B. 2005, *ApJS*, **160**, 115
- Sahu, M. S. 1998, *AJ*, **116**, 1205
- Sakai, S., Ferrarese, L., Kennicutt, R. C., & Saha, A. 2004, *ApJ*, **608**, 42
- Savage, B. D., et al. 2000, *ApJS*, **129**, 563
- Savaglio, S., et al. 2004, *ApJ*, **602**, 51
- Schiavon, R. P. 2007, *ApJS*, **171**, 146
- Schlegel, D. J., Finkbeiner, D. P., & Davis, M. 1998, *ApJ*, **500**, 525
- Schwartz, C. M., Martin, C. L., Chandar, R., Leitherer, C., Heckman, T. M., & Oey, M. S. 2006, *ApJ*, **646**, 858
- Schweizer, F., et al. 2008, *AJ*, **136**, 1482
- Seitz, S., Saglia, R. P., Bender, R., Hopp, U., Belloni, P., & Ziegler, B. 1998, *MNRAS*, **298**, 945
- Shapley, A. E., Steidel, C. C., Adelberger, K. L., Dickinson, M., Giavalisco, M., & Pettini, M. 2001, *ApJ*, **562**, 95
- Shapley, A. E., Steidel, C. C., Pettini, M., & Adelberger, K. L. 2003, *ApJ*, **588**, 65
- Siana, B., Teplitz, H. I., Chary, R.-R., Colbert, J., & Frayer, D. T. 2008, *ApJ*, **689**, 59
- Soifer, B. T., Boehmer, L., Neugebauer, G., & Sanders, D. B. 1989, *AJ*, **98**, 766
- Spergel, D. N., et al. 2007, *ApJS*, **170**, 377
- Steidel, C. C., Pettini, M., & Adelberger, K. L. 2001, *ApJ*, **546**, 665
- Teplitz, H. I., et al. 2000, *ApJ*, **533**, L65
- Thuan, T. X. 1983, *ApJ*, **268**, 667
- Thuan, T. X., Lipovetsky, V. A., Martin, J.-M., & Pustilnik, S. A. 1999, *A&AS*, **139**, 1
- Tosi, M., Sabbi, E., Bellazzini, M., Aloisi, A., Greggio, L., Leitherer, C., & Montegrippo, P. 2001, *AJ*, **122**, 1271
- Tremonti, C. A., Calzetti, D., Leitherer, C., & Heckman, T. M. 2001, *ApJ*, **555**, 322
- van Zee, L., Salzer, J. J., Haynes, M. P., O'Donoghue, A. A., & Balonek, T. J. 1998, *AJ*, **116**, 2805
- Vázquez, G. A., Leitherer, C., Heckman, T. M., Lennon, D. J., de Mello, D. F., Meurer, G. R., & Martin, C. L. 2004, *ApJ*, **600**, 162
- Vink, J. S., de Koter, A., & Lamers, H. J. G. L. M. 2001, *A&A*, **369**, 574
- Weedman, D. W., Feldman, F. R., Balzano, V. A., Ramsey, L. W., Sramek, R. A., & Wu, C. C. 1981, *ApJ*, **248**, 105
- Worthey, G. 1994, *ApJS*, **95**, 107